Spatial Resolved Electronic Structure of Low Dimensional Materials and Data Analysis

Han Peng

The Queen's College
University of Oxford

A thesis submitted for the degree of
Doctor of Philosophy

Trinity 2018

Abstract

Two dimensional (2D) materials with interesting fundamental physics and potential applications attract tremendous efforts to study. The versatile properties of 2D materials can be further tailored by tuning the electronic structure with the layer-stacking arrangement, of which the main adjustable parameters include the thickness and the in-plane twist angle between layers. The Angle-Resolved Photoemission Spectroscopy (ARPES) has become a canonical tool to study the electronic structure of crystalline materials. The recent development of ARPES with sub-micrometre spatial resolution (micro-ARPES) has made it possible to study the electronic structure of materials with mesoscopic domains. In this thesis, we use micro-ARPES to investigate the spatially-resolved electronic structure of a series of few-layer materials:

1. We explore the electronic structure of the domains with different number of layers in few-layer graphene on copper substrate. We observe a layer-dependent substrate doping effect in which the Fermi surface of graphene shifts with the increase of number of layers, which is then explained by a multilayer effective capacitor model.

2. We systematically study the twist angle evolution of the energy band of twisted few-layer graphene over a wide range of twist angles (from 5° to 31°). We directly observe van Hove Singularities (vHSs) in twisted bilayer graphene with wide tunable energy range over 2 eV. In addition, the formation of multiple vHSs (at different binding energies) is observed in trilayer graphene. The large tuning range of vHS binding energy in twisted few-layer graphene provides a promising material base for optoelectrical applications with broad-band wavelength selectivity.

3. To better extract the energy band features from ARPES data, we propose a new method with a convolutional neural network (CNN) that achieves comparable or better results than traditional derivative based methods.

Besides ARPES study, this thesis also includes the study of surface reconstruction for the layered material Bi_2O_2Se with the analysis of Scanning Tunnelling Microscopy (STM) images. To explain the origin of the pattern, we propose a tile model that produces the identical statistics with the experiment.

Spatial Resolved Electronic Structure of Low Dimensional Materials and Data Analysis

Han Peng

The Queen's College

University of Oxford

A thesis submitted for the degree of

Doctor of Philosophy

Trinity 2018

This thesis is dedicated to
my parents, Huihua Peng and Chiying Liao

Acknowledgements

I would like to thank Cheng Chen, Yiwei Li and Dr Chaofan Zhang for proofreading the chapters. I would also like to thank Prof Marcin Mucha-Kruczynski and Prof Stephen Blundell for acting as examiners of this thesis.

I would like to express my gratitude to my DPhil supervisor, Prof Yulin Chen. Under his guidance, I grow from an undergraduate student towards a researcher. He has been a great mentor who respects my ideas and encourages me to develop my own research interest.

I am grateful to my fellow colleagues in Oxford Chen group: Niels Schroeter, Cheng Chen, Sandy Ekahana, Yiwei Li and Ding Pei for their help and companion. I will miss our stimulating discussions and the post-experiment dinners. I am also grateful to other members of Chen group around the world, especially Dr Juan Jiang, Dr Haifeng Yang, Dr Chaofan Zhang, Prof Zhongkai Liu, Prof Lexian Yang, for their help and advice on my research projects.

Besides Chen group, I am also grateful to the help received from my collaborators. I would like to thank Dr Jianbo Yin and Prof Hailin Peng from Peking University for their important advice on the graphene project so that the manuscript could be finally published. I would also like to acknowledge Xiang Gao from University of Florida for his help in the convolutional neural network project.

There are up and downs in the last four years and not all the projects are fruitful. I spent most of my third year of DPhil in finding out the origin of some mysterious ARPES signal. Thanks to Dr Shilei Zhang in the department, Dr Huixia Fu and Prof Binghai Yan who are from Weizmann Institute of Science, we finally figured out that the signal was from a less interesting compound. This result, though not as promising as the project seemed to be at the beginning, largely pacified my curiosity, and solving puzzles is all the fun a nice DPhil experience has to offer.

In the wider academia community, I would like to thank Prof Ning Xu, who is from School of Physics in University of Science and Technology of China, for his precious advice on research form the perspective of a computational physicist.

I would like to especially thank Prof Kenneth Harris, with whom I did a summer research in neural science data analysis in 2017, for his patience and guidance. Kenneth not only showed me a broader view of scientific methodology used in a different branch of science, but also provides me a role model as a great mentor and scholar.

Outside the academia life, I have many thanks to Penglin Cai, Yiwei Li, Xuelian Liu, Tian Zhang, and many other friends in Oxford who helped me to achieve the daily goal of having dinner with other human beings. I also want to thank Zhiming Zhou, my dearest friend, for stopping me from a 'quick descend' of 1,200 metres down the east ridge of Aiguille du Midi in the summer of 2015, after I was tripped by my own crampons. Slightly confused about the future direction at that time (with mid-PhD crisis?), I decided to climb mountains and run marathons to provide my dopamine system with continuous positive feedback. Luckily, I gave up my Mont Blanc plan in 2015 after the fell (and did it in 2016 after one-year training).

Special gratitude goes to my girlfriend Ganlu Zhou who oversees me to stick to the writing schedule for my thesis. Every character in this thesis is typed in through the keyboard you sent me.

I would never complete this thesis without the support from my family, both mentally and financially. My parents and grandparents have always provided me the best education opportunities they could give, as well as the freedom to explore my own interests, ambitions and plans, not to mention that my mom spent multiples of her monthly salary to buy the GTX1080ti GPU, an expensive gift she would never buy for herself, for me to train the neural network without delay for Chapter 4. I would like to share all my joy with them in finishing this thesis. I wish my mom's father could be able to share this moment with us together. He passed away suddenly in the first month of my time at Oxford in the summer of 2013. I wish I could have said goodbye to him.

Abstract

Two dimensional (2D) materials with interesting fundamental physics and potential applications attract tremendous efforts to study. The versatile properties of 2D materials can be further tailored by tuning the electronic structure with the layer-stacking arrangement, of which the main adjustable parameters include the thickness and the in-plane twist angle between layers. The Angle-Resolved Photoemission Spectroscopy (ARPES) has become a canonical tool to study the electronic structure of crystalline materials. The recent development of ARPES with sub-micrometre spatial resolution (micro-ARPES) has made it possible to study the electronic structure of materials with mesoscopic domains. In this thesis, we use micro-ARPES to investigate the spatially-resolved electronic structure of a series of few-layer materials:

1. We explore the electronic structure of the domains with different number of layers in few-layer graphene on copper substrate. We observe a layer-dependent substrate doping effect in which the Fermi surface of graphene shifts with the increase of number of layers, which is then explained by a multilayer effective capacitor model.

2. We systematically study the twist angle evolution of the energy band of twisted few-layer graphene over a wide range of twist angles (from 5° to 31°). We directly observe van Hove Singularities (vHSs) in twisted bilayer graphene with wide tunable energy range over 2 eV. In addition, the formation of multiple vHSs (at different binding energies) is observed in trilayer graphene. The large tuning range of vHS binding energy in twisted few-layer graphene provides a promising material base for optoelectrical applications with broad-band wavelength selectivity.

3. To better extract the energy band features from ARPES data, we propose a new method with a convolutional neural network (CNN) that achieves comparable or better results than traditional derivative based methods.

Besides ARPES study, this thesis also includes the study of surface reconstruction for the layered material Bi_2O_2Se with the analysis of Scanning Tunnelling Microscopy (STM) images. To explain the origin of the pattern, we propose a tile model that produces the identical statistics with the experiment.

Publication List

Graphene and low-dimension materials

1. **H. Peng**†, N. B. M. Schröter†, J. B. Yin, H. Wang, T.-F. Chung, H. F. Yang, S. Ekahana, Z. K. Liu, J. Jiang, L. X. Yang, T. Zhang, C. Chen, H. Ni, H. Barinov, Y. P. Chen, Z. F. Liu, H. L. Peng, Y. L. Chen "Substrate Doping Effect and Unusually Large Angle van Hove Singularity Evolution in Twisted Bi- and Multilayer Graphene" ***Advanced Materials, 29, 27*** (2017)

2. J. B. Yin†, H. Wang†, **H. Peng**†, Z. J. Tan, L. Liao, L. Lin, X. Sun, A. L. Koh, Y. L. Chen, H. L. Peng, and Z. F. Liu "Selectively enhanced photocurrent generation in twisted bilayer graphene with van Hove singularity" ***Nature Communications, 7, 10699*** (2016)

3. L. Liao, H. Wang, **H. Peng**, J. B. Yin, A. L. Koh, Y. L. Chen, Q. Xie, H. L. Peng, and Z. F. Liu "van Hove Singularity Enhanced Photochemical Reactivity of Twisted Bilayer Graphene" ***Nano Letters, 15, 5585*** (2015)

4. H. F. Yang, C. Chen, H. Wang, Z. K. Liu, T. Zhang, **H. Peng**, N. B. M. Schröter, S. A. Ekahana, J. Jiang, L. X. Yang, V. Kandyba, A. Barinov, C. Y. Chen, J. Avila, M. C. Asensio, H. L. Peng, Z. F. Liu, and Y. L. Chen "Single Crystalline Electronic Structure and Growth Mechanism of Aligned Square Graphene Sheets" ***APL Materials 6, 036107*** (2018), featured on the cover

5. C. Chen, M. X. Wang,J. X. Wu, Y. Sun, H. F. Yang, Z. Tian, T. Tu, **H. Peng**, G. Li, H. X. Fu, X. Xu, J. Jiang, N. B. M. Schroeter, Y. W. Li, D. Pei, S. Liu, S. Ekahana, H. T. Yuan, J. M. Xue, Z. K. Liu, B. H. Yan, H. L. Peng and Y. L. Chen "Electronic Structures of a High-Mobility Layered Oxychalcogenide Semiconductor, Bi_2O_2Se" ***Manuscript under peer-review***

Data analysis

6. **H. Peng**, X. Gao, Y. He, Z. K. Liu, Y. L. Chen "Super Resolution Convolutional Neural Network for Feature Extraction in Spectroscopic Data" ***Manuscript ready to submit***

7. S. L. Zhang, W. W. Wang, D. M. Burn, **H. Peng**, H. Berger, A. Bauer, C. Pfleiderer, G. van der Laan, and T. Hesjedal " Manipulation of Skyrmion Motion by Magnetic Field Gradients" ***Nature Communications, accepted***

Other ARPES projects

8. J. Jiang, N. B. M. Schröter, S.-C. Wu, N. Kumar, C. Shekhar, **H. Peng**, X. Xu, C. Chen, H. F. Yang, C.-C. Hwang, S.-K. Mo, C. Felser, B. H. Yan, Z. K. Liu, L. X. Yang, and Y. L. Chen "Observation of topological surface states and strong electron/hole imbalance in extreme magnetoresistance compound LaBi" ***Physical Review Materials, 2, 024201*** (2018)

9. A. J. Liang, J. Jiang, M. X. Wang, Y. Sun, N. Kumar, C. Shekhar, C. Chen, **H. Peng**, C. W. Wang, X. Xu, H. F. Yang, S. T. Cui, G. H. Hong, Y. Y. Y. Xia, S. K. Mo, Q. Gao, X. J. Zhou, L. X. Yang, C. Felser, B. H. Yan, Z. K. Liu, Y. L. Chen 2017. Observation of the topological surface state in the nonsymmorphic topological insulator KHgSb. ***Physical Review B, 96(16), p.165143*** (2017)

10. J. Jiang, Z. K. Liu, Y. Sun, H. F. Yang, R. Rajamathi, Y. P. Qi, L. X. Yang, C. Chen, **H. Peng**, C.-C. Hwang, S. Z. Sun, S.-K. Mo, I. Vobornik, J. Fujii, S. S. P. Parkin, C. Felser, B. H. Yan, Y. L. Chen "Signature of type-II Weyl semimetal phase in $MoTe_2$" ***Nature Communications, 8, 13973*** (2017)

11. Z. K. Liu, L. X. Yang, Y. Sun, T. Zhang, **H. Peng**, H. F. Yang, C. Chen, Y. Zhang, Y. F. Guo, D. Prabhakaran, M. Schmidt, Z. Hussain, S.-K. Mo, C. Felser, B. Yan and Y. L. Chen "Evolution of the Fermi surface of Weyl semimetals in the transition metal pnictide family" ***Nature Materials, 15, 27*** (2016)

12. L. X. Yang, Z. K. Liu, Y. Sun, **H. Peng**, H. F. Yang, T. Zhang, B. Zhou, Y. Zhang, Y. F. Guo, M. Rahn, D Prabhakaran, Z. Hussain, S.–K. Mo, C. Felser, B. Yan and Y. L. Chen "Weyl Semimetal Phase in non-Centrosymmetric Compound TaAs" ***Nature Physics, 11, 728*** (2015)

13. Z. K. Liu, J. Jiang, B. Zhou, Z. J. Wang, Y. Zhang, H. M. Weng, D. Prabhakaran, S. -K. Mo, **H. Peng**, P. Dudin, T. Kim, M. Hoesch, Z. Fang, X. Dai, Z. X. Shen, D. L. Feng, Z. Hussain, Y. L. Chen. "A Stable Three-dimensional Topological Dirac Semimetal Cd_3As_2" ***Nature Materials, 13, 677*** (2014)

† Equal contribution authors

Contents

List of Figures

1

Introduction to Angle-Resolved Photoemission Spectroscopy (ARPES)

Contents

1.1 Photoemission experiment

Photoemission experiments have a long history that dates back to Hertz's experiment in 1887 and remains as an important method in condensed matter physics [1]. The recent development of Angle-Resolved Photoemission Spectroscopy (ARPES) technique provides a powerful tool to resolve the energy bands in crystal samples, which plays an important role in revealing the physics in superconductors [2], topological materials [3, 4] and low dimensional materials [5, 6].

The principle of ARPES experiment is illustrated in Figure 1.1. A photon beam is focused on the sample surface to induce emitted photoelectrons, which are then collected by the energy analyser with a finite acceptance range of angles [2].

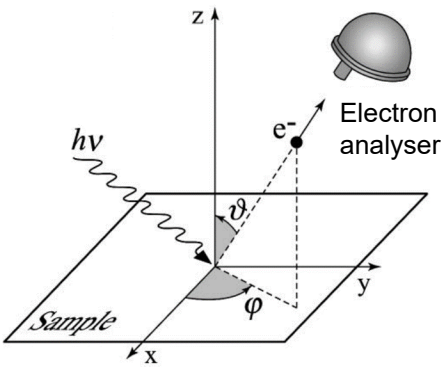

Figure 1.1: Illustration of ARPES experimental setup. Image adapted reproduced from Reference [2] with permission of the rights holder, American Physical Society.

The direction of the electron momentum and the kinetic energy is recorded by the analyser. Under an non-interacting picture, we could use the energy conservation in the photoemission process and the binding energy E_b of the initial state for the electrons can be inferred from the relation

$$E_K = h\nu - \Phi - |E_b|$$

The total momentum of the photoelectron is

$$|\boldsymbol{p}| = \hbar|\boldsymbol{k}| = \sqrt{2mE_K}$$

The momentum component that is parallel to the sample surface ($k_\parallel$) is also conserved so that the parallel component of crystal momentum can be inferred:

$$\begin{cases} k_x = |\boldsymbol{k}|\sin(\theta)\cos(\phi) \\ k_y = |\boldsymbol{k}|\sin(\theta)\sin(\phi) \end{cases} \tag{1.1}$$

The perpendicular component of the momentum (k_z) is not conserved due to the existence of the crystal surface potential. To figure out k_z, additional assumption of the effective mass m_{eff} and the crystal potential V_0 are needed to fit the experiment data with the relation as describe in the supplementary material in References [7, 8]:

$$\hbar^2(k_x^2 + k_y^2 + k_z^2) = 2m_{eff}(E_K + V_0)$$

In the real physical system, the photoemission process should be treated under the framework of many-body physics due to the interactions. In this scenario,

the detected energy band has a finite peak width. The outline below can be found in detail from Reference [2].

To model the photoemission process, a 'three-step model' is widely used. It decomposes the process as three stages:

1. The photon excites an electron inside the sample bulk.
2. The excited electron travels from the bulk to the surface.
3. The excited electron escapes into vacuum.

While the second step can be described as a mean free path and the third step by the surface potential barrier Φ, the first step carries the physical information detected by the photon beam and determines the photoelectron count $I(k, E_K)$ by the ARPES energy analyser, which is proportional to the transfer probability calculated by Fermi's golden rule between the initial state i and the final state f:

$$I(k, E_K) \propto \sum_{fi} w_{fi} \propto \sum_{fi} |\langle \Psi_f^N | H_{int} | \Psi_i^N \rangle|^2 \delta(E_f^N - E_i^N - h\nu)$$

where Ψ_f^N and Ψ_i^N are the final and the initial N-particle state, respectively.

Assuming the excited photon does not interacted with the rest of the system (sudden approximation) and Ψ_f^N (Ψ_i^N) can be factorized as a product of one particle wave function and the rest of N-1 particle system $C[\phi_f(\boldsymbol{k})\Psi_f^{N-1}]$ ($C[\phi_i(\boldsymbol{k})\Psi_i^{N-1}]$), where C is the antisymmetrization operator, the intensity can be further written as

$$I(k, E_K) \propto \sum_{fi} |\langle \phi_f(\boldsymbol{k}) | H_{int} | \phi_i(\boldsymbol{k}) \rangle|^2 \sum_m |\langle \Psi_m^{N-1} | \Psi_i^{N-1} \rangle|^2 \delta(E_m^{N-1} + E_K - E_i^N - h\nu)$$

where Ψ_m^{N-1} is the eigenfunction for the excited state. The first part of the product is called matrix element $\sum_{fi} M_{fi}^{\boldsymbol{k}}$ which specifies the light-matter interaction. The second half can be further calculated using the Green's-function formalism with a proper self-energy $\Sigma = \Sigma' + i\Sigma''$ and considering the Fermi-Dirac distribution $f(E) = 1/(\exp(\frac{E-E_F}{k_B T} + 1)$

$$I(\boldsymbol{k}, E) \propto \sum_{fi} M_{fi}^{\boldsymbol{k}} f(E) A(\boldsymbol{k}, E_K)$$

where

$$A(\boldsymbol{k}, E) = \frac{1}{\pi} \frac{\Sigma''}{(E - \epsilon(\boldsymbol{k}) - \Sigma')^2 + \Sigma''^2}$$

1.2 ARPES system

As described in Reference [2] and shown in Figure 1.2, the ARPES set-up consists of three major parts: the light source, the high-vacuum chamber, and the electron energy analyser.

The state-of-the-art ARPES benefits from the synchrotron radiation, as it provides wide-range photon-energy (e.g. 18 eV to 240 eV at Beamline I05, Diamond Light Source [9]), high intensity and highly polarized light source so that the $z-$direction of the momentum space can be explored with high efficiency.

Due to the surface sensitivity of the ARPES experiment, the bulk-crystal sample is often cleaved in-situ to produce fresh flat surface in high-vacuum environment (usually better than 10^{-10} torr). For thin films that cannot be cleaved, annealing and sputtering is often used to produce good crystal surface. The high-vacuum environment is maintained to protect the surface from degrading.

The photoelectrons emitted from the sample surface are then collected by the electron energy analyser. The modern hemispherical anlyser can record a 2D energy-momentum map at one single measurement. As shown in Figure 1.2, the electrons with different momentum directions (θ_x) are focused through electrostatic lens at different positions on the entrance slit of the analyser. Then the electrons with different kinetic energy are differentiated using the electric field in-between the two concentric hemispheres. To obtain a full 3D $k_x - k_y - E$ mapping of the energy band, either the analyser or the sample is rotated by a small angle θ_y, so that another 2D energy-momentum map can be added to the image stack.

1.3 ARPES with micrometre spatial resolution

ARPES provides a powerful tool to reveal the energy band structures of crystal samples. However, a regular ARPES has a very limited real-space resolution with its beam spot size (typically $> 100\,\mu$m). This limitation puts constrains on the choice of samples that is compatible with the ARPES measurement: only large crystalline sample with large and flat cleavage planes can produce ideal signals, otherwise the

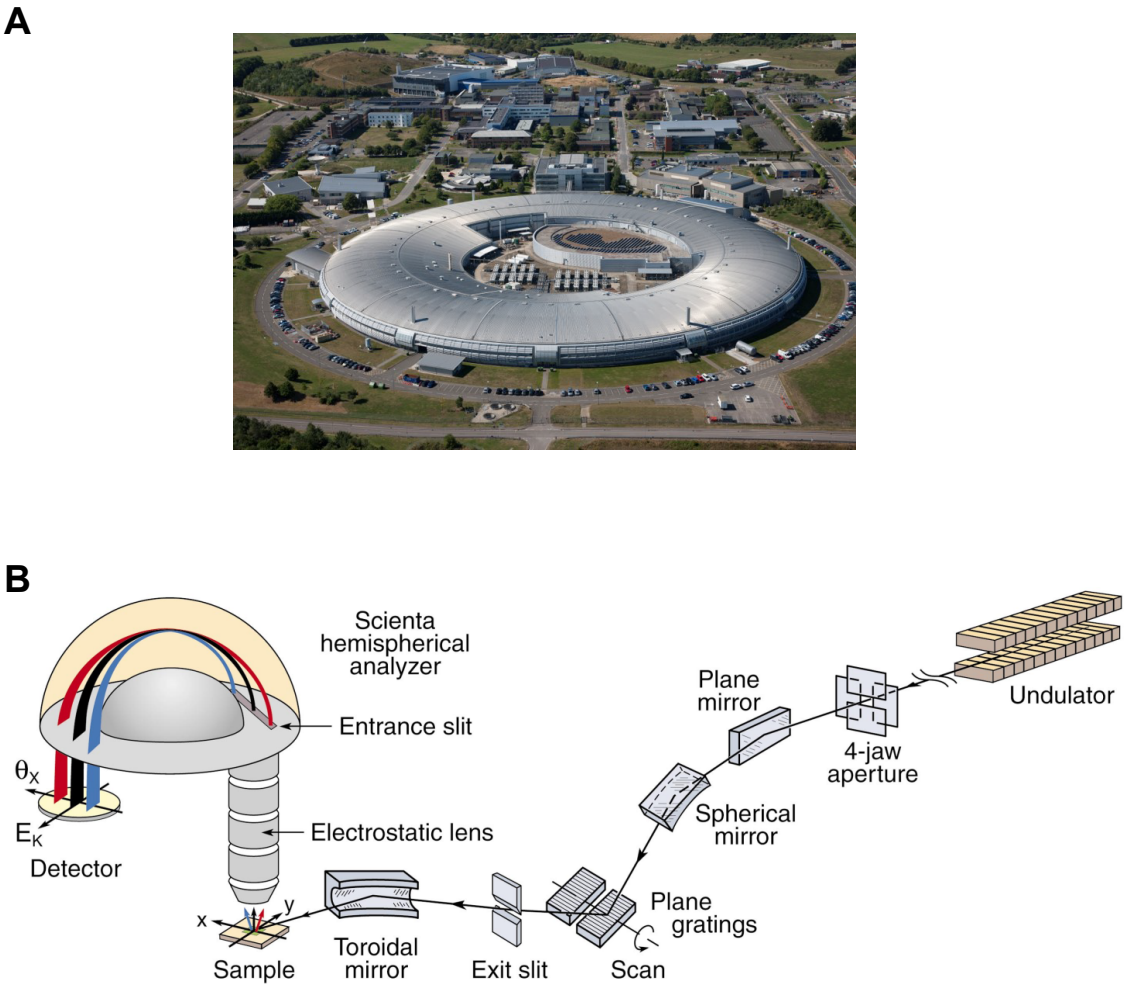

Figure 1.2: Illustration of ARPES system. A. Photo of a synchrochon light source, Diamond Light Source. Photo is used with the permission of the rights holder, Diamond Light Source. **B.** Image adapted reproduced from Reference [2] with the permission of the rights holder, American Physical Society.

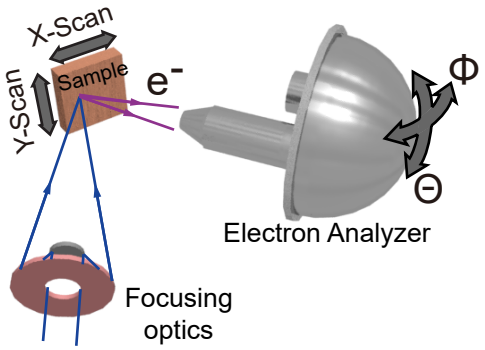

Figure 1.3: Illustration of micro-ARPES operational principle. Rotating the analyser along Θ and Φ direction probes momenta in reciprocal space, while moving the sample along X and Y direction probes different positions in real space. Either a Schwarzschild mirror (as shown here) or a Fresnel zone plate achieves micro focusing of the synchrotron light.

beam spot will cover multiple sample domains and produce an average signal from different areas. Moreover, the recent advancement of low-dimensional materials tend to produce spatially varying sample morphology. The ability to resolve different electronic structure in different part of the sample is needed to study these materials. Fortunately, the recent development of ARPES with micrometre spatial resolution (micro-ARPES) enables us to overcome this drawback.

As shown in Figure 1.4, micro-ARPES has a much smaller beam spot that allows one to focus in a domain and to resolve the electronic structure locally for twisted few-layer graphene.

The principle of micro-ARPES is illustrated in Figure 1.3, where the photon beam from the synchrotron beamline is focused onto the sample down to a spot size less than 1 µm in diameter (e.g. ~ 0.8 µm at Spectromicroscopy-3.2 L beamline of Elettra [10]). At a given sample position, the electron analyser can rotate around two axes to collect the electronic band structure ; and the sample can be scanned along two directions (X and Y directions) in the real space, thus the band structure at different sample locations can be investigated.

In the real-space scan mode, the angle between the sample and the analyser will be fixed, while the sample is moving along the X and Y directions consecu-

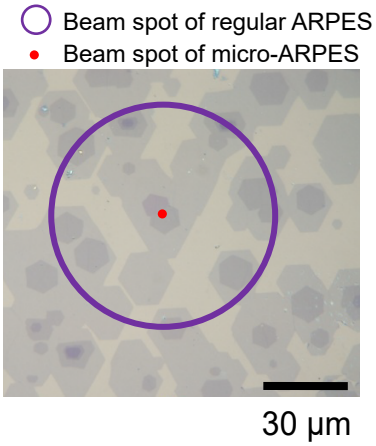

Figure 1.4: Illustration of typical beam spot sizes on the domains of twisted few-layer graphene. The purple circle shows the beam spot of a regular ARPES and the red dot illustrates that of a micro-ARPES. The regular ARPES beam size (larger than 100 µm) covers multiple domains in one measurement, while the micro-ARPES can focus on a local spot. The image is taken with an optical microscope.

tively so the photon beam scans through the sample surface. The photoelectrons from different positions are gathered by the analyser. A two-dimensional energy-momentum dispersion map is recorded ($k - E$) for each real-space position, making the experimental data 4-dimensional ($X - Y - k - E$). The areas belonging to the same domain tends to possess homogeneous band structure, while the areas from the different domains differ in the electronic structure. For example, Figure 1.5 shows a typical real-space scan data set of graphene on top of copper substrate. The raw 4-dimensional data is projected into the two dimensions of the real space, producing the intensity contrast between the graphene-covered area and the bare copper area. By retrieving the energy-momentum dispersion map in different positions, we find a copper signal from both dark and bright area, while the graphene signal is only found on the dark side.

After the real-space scan, energy-momentum mapping can be performed at each region of interest and collect the typical 3D ARPES mapping data ($k_x - k_y - E$).

With the spatial resolving ability of micro-ARPES, we are able to identify different sample domains in few-layer graphene as presented in Chapter 2. By performing

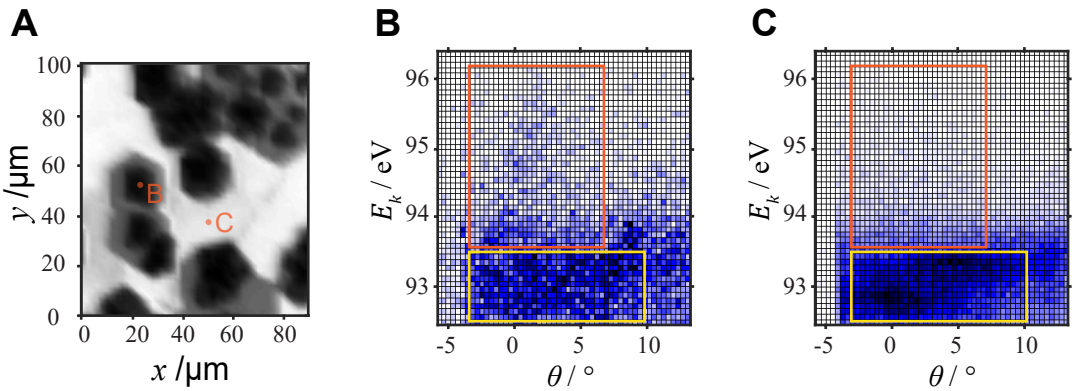

Figure 1.5: A typical micro-ARPES 4D data set of graphene on copper substrate. A. The projection of the 4D data set into the real space by integrating the intensities over the other two dimensions (momentum and energy). **B. and C.** Raw data showing electronic energy band structure in position B and C marked in A, respectively. The horizontal axis is the angle and the vertical axis is the kinetic energy recorded by the analyser. The angle can be converted to the corresponding momentum in the subsequent data analysis pipeline. The orange boxes mark the area with the appearance of the energy band of graphene and the yellow boxes mark the energy band of copper.

fine measurement of the electronic structures in each region of interest, we study the energy band evolution with twist angle in twisted bilayer graphene in Chapter 3.

1.4 ARPES data analysis and its challenges

The recent development of ARPES technique not only enhances the data resolution and adds new dimensions to the measurements, but also requires new data analysis methods that are able to deal with large scale data with high speed.

As illustrated in Figure 1.1, the angles of the momentum (θ and ϕ in the spherical coordinate system) and the kinetic energy (E_k) are recorded for the photoelectrons. Thus, the raw data of energy-momentum mapping resides in the angle space (θ and ϕ). The first step of the data analysis pipeline is to convert the intensities recorded at the coordination (θ, ϕ, E_k) (angle-space) to the coordination (k_x, k_y, E_k) (k-space), following Equation 1.1:

$$\begin{cases} k_x = |\boldsymbol{k}|\sin(\theta)\cos(\phi) \\ k_y = |\boldsymbol{k}|\sin(\theta)\sin(\phi) \end{cases} \tag{1.2}$$

This process is called k-space-conversion. Though the coordination transform is straightforward, the realization of the algorithm needs special care to accelerate the speed for real-time processing during experiments. A naive realization of the algorithm that grids the data into a 3D mesh can be too slow to perform on-the-fly data analysis.

Given that the chunk of raw data for k-space mapping is recorded and stored in a 3D grid specified by (θ, ϕ, E_k) and the k-converted data in a new grid specified by (k_x, k_y, E_k), the two grids do not match layer-wise along the first two dimensions due to the non-linear transform specified by Equation 1.1. Thus, interpolation is needed to re-grid each layer after converting the angle-coordinates to k-coordinates for each voxel in the raw data. A naive conversion algorithm will do one interpolation for each layer. This method will be slow for a modern ARPES data set as the typical size of the data set is $(n_\theta, n_\phi, n_E) \sim (1000, 200, 1000)$ and it requires $n_E = 1000$ times of interpolations. Indeed, the time spent for each data set is in the order of 10 minutes.

Special treatment can be used to accelerate the k-space conversion process by using the similarities of the data shared within each layer. Revisiting Equation 1.1, we find that the k-converted coordinates for each equal-energy layer only differs by a factor $|\boldsymbol{k}| = \sqrt{2mE_k}/\hbar$. Thus, we could interpolate each (θ, ϕ) layer in the same new grid $(k_x/|\boldsymbol{k}|, k_y/|\boldsymbol{k}|)$ and finalize the result by 'stretching' each layer to the final grid (k_x, k_y). Using this method, the algorithm takes only about ten seconds for a typically sized data set in a consumer laptop with an Intel i7-7700HQ cpu.

Another technical challenge is that the cleavage surface normal may not coincide with the $z-$direction defined by the equipment set-up. In this case, the correct surface normal needs to be identified so that the parallel momentum component $k_\parallel$ can be retrieved from the data. As shown by the example data in Figure 1.6.A, the Brillouin zones (BZs) can be identified but the arrangement is distorted. A correct k-space conversion should recover the periodic pattern of the BZs (as shown in Figure 1.6.B). If the normal direction is not too far away from $z-$direction, then it could be guessed by the symmetry of the data set and then confirmed by photon-energy-changing measurements. In other cases, it requires multiple times of

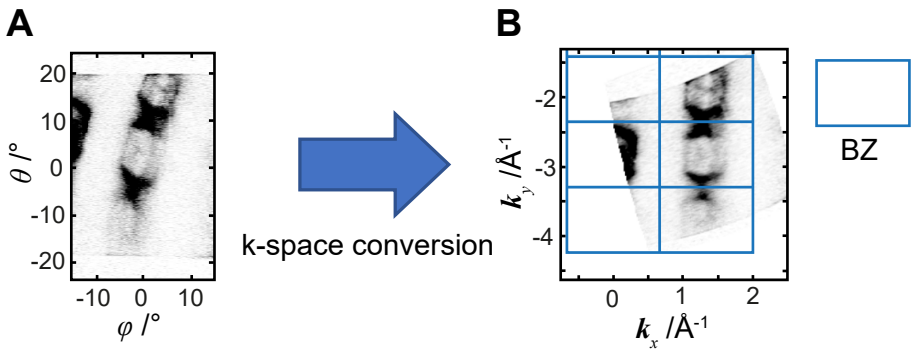

Figure 1.6: A typical equal energy surface measured from highly tilted sample cleavage plane. A. An equal energy surface sliced from the raw data in an ARPES measurement of GdPtBi 110 surface. Unlike the 111 surface of GdPtBi [11], the 110 cleavage plane is highly tilted so that the Brillouin zones are curved. **B.** The k-converted equal energy surface from the raw data shown in A. The cleavage surface normal direction (first-Γ point in k-space) is guessed and tested for multiple times to obtain the correct k-space conversion result. The blue rectangles are the surface projected Brillouin zones of GdPtBi 110 plane.

trial-and-error process to find the surface normal with the assistance of a graphic user interface and the accelerated k-space conversion algorithm.

As the bottleneck of data processing speed is unblocked, a greater challenge is to retrieve physical information from the noisy and blurry data. As shown in Figure 1.7, two energy bands are too close to each other and cannot be segregated. By analysing the momentum distribution curves (MDCs, shown in Fiugre 1.7.B) and energy ditribution curves (EDCs, shown in Fiugre 1.7.C) carefully, one could fit the peaks with prior knowledge of the peak shape and trace the energy bands. However, MDC/EDC fitting uses only the information along one-dimension of data and the assumed peak shape can be affected by many other factors [12]. To solve this problem, we propose a neural network based method, which is described in detail in Chapter 4.

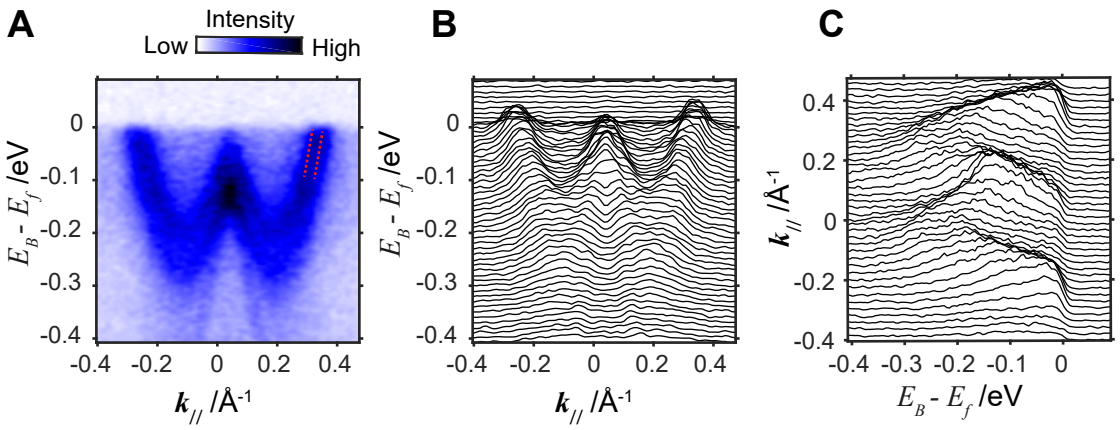

Figure 1.7: A typical energy-momentum dispersion map from NbAs. A. The energy-momentum dispersion intensity plot of data taken from NbAs [13]. The two dashed lines suggest two energy bands that are close to each other. **B.** The momentum density curves (MDC) plotted in stacks. **C.** The energy density curves (EDC) plotted in stacks.

Bibliography

[1] Stephan Hüfner. *Photoelectron spectroscopy: principles and applications*. Springer Science & Business Media, 2013.

[2] Andrea Damascelli, Zahid Hussain, and Zhi-Xun Shen. "Angle-resolved photoemission studies of the cuprate superconductors". In: *Reviews of modern physics* 75.2 (2003), p. 473.

[3] YL Chen et al. "Experimental realization of a three-dimensional topological insulator, Bi_2Te_3". In: *Science* 325.5937 (2009), pp. 178–181.

[4] M Zahid Hasan and Charles L Kane. "Colloquium: topological insulators". In: *Reviews of Modern Physics* 82.4 (2010), p. 3045.

[5] Taisuke Ohta et al. "Controlling the electronic structure of bilayer graphene". In: *Science* 313.5789 (2006), pp. 951–954.

[6] Mattia Cattelan and Neil A Fox. "A Perspective on the Application of Spatially Resolved ARPES for 2D Materials". In: *Nanomaterials* 8.5 (2018).

[7] ZK Liu et al. "Discovery of a three-dimensional topological Dirac semimetal, Na_3Bi". In: *Science* 343.6173 (2014), pp. 864–867.

[8] ZK Liu et al. "A stable three-dimensional topological Dirac semimetal Cd_3As_2". In: *Nature Materials* 13.7 (2014), p. 677.

[9] M Hoesch et al. "A facility for the analysis of the electronic structures of solids and their surfaces by synchrotron radiation photoelectron spectroscopy". In: *Review of Scientific Instruments* 88.1 (2017), p. 013106.

[10] Pavel Dudin et al. "Angle-resolved photoemission spectroscopy and imaging with a submicrometre probe at the SPECTROMICROSCOPY-3.2 L beamline of Elettra". In: *Journal of Synchrotron Radiation* 17.4 (2010), pp. 445–450.

[11] Chang Liu et al. "Metallic surface electronic state in half-Heusler compounds R PtBi (R= Lu, Dy, Gd)". In: *Physical Review B* 83.20 (2011), p. 205133.

[12] Yu He, Yan Wang, and Zhi-Xun Shen. "Visualizing dispersive features in 2D image via minimum gradient method". In: *Review of Scientific Instruments* 88.7 (2017), p. 073903.

[13] HF Yang et al. "Topological Lifshitz transitions and Fermi arc teleportation". In: *Manuscript under peer review* (2018).

2

ARPES with micrometre spatial resolution in few-layer system

Contents

Using the spatial scanning ability of micro-ARPES, we are able to explore the electronic structure of the domains with different number of layers in a few-layer graphene on a copper substrate. We directly observe the attenuation of photoelectron from the substrate, with an average penetration depth of 1.3 layers. By checking the Fermi surfaces of graphene domains with different number of layers, we observe a thickness-dependent substrate doping effect, which we explain by a multilayer effective capacitor model.

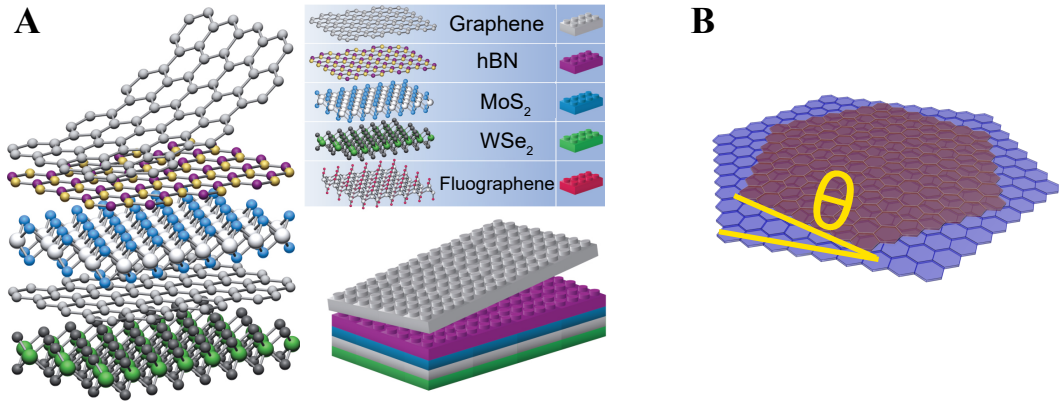

Figure 2.1: Stacking of two-dimensional materials. A. The choice of materials and the stacking order of the layers provide a large parameter space to explore. Image adapted from Reference [1] with permission of the rights holder, Springer Nature. **B.** The twist angle among layers provides an additional degree of freedom to tune the electronic structures of few-layer materials.

2.1 Introduction

2.1.1 Introduction to van der Waals heterostructures

The discovery of graphene and other two dimensional atomic crystals not only provides a platform to observe novel quantum phenomenon but also enables the possibility of producing high-performance low-dimensional devices [2–5]. When stacking multiple 2D crystal layers together, the van der Waals interaction among layers allows to further engineer the electronic structures for the thin films [1]. As shown in Figure 2.1, the type of chosen materials, the order of arrangement and the twist angle of stacking provide additional degrees of freedom to enhance the electronic properties for the few-layer system, while giving us a huge parameter space to explore. Systematic study in the energy band structure of multilayer system is required to achieve better understanding of the dependence of electronic properties in these tuning parameters.

ARPES has been a powerful tool to study the band structure of crystals including graphene [6], layered transition metal dichalcogenides [7], and other low-dimensional materials. However, the poor spatial resolution (typically hundreds of micrometres) limits its ability to further resolve the electronic structure in these few-layer materials. As illustrated in Figure 1.4, the grain size of CVD grown few-layer graphene is

typically up to tens of micrometres, while the hundred-micrometre sized beam spot of a regular ARPES covers multiple domains in one measurement. As a result, the photoelectrons collected by a regular ARPES could be from different spatial domains of the sample, making the detected signals a mixture of different band structures.

Fortunately, the recent development of ARPES with sub-micrometre spatial resolution (i.e. micro-ARPES) [8, 9] provides an excellent tool for this study. The capability of obtaining complete electronic structures of samples down to 1 µm enables us to investigate and to compare these domains with varying twist angles, layer numbers and different type of materials.

In this chapter, we use the few-layer graphene on copper substrate as an example system to demonstrate the spatial resolution of micro-ARPES. We systematically study the photoemission intensity dependence on the layer numbers and use this effect to visualise the sample morphology. Using the ability of micro-ARPES to resolve the electronic structure of local domains, we report a layer-dependent substrate doping effect, i.e. the Ferimi surface shift of the thin films due to the electrons transferred from the substrate. This effect is then explained by an effective capacitor model for a multilayer system.

2.1.2 Introduction to graphene band structure

Graphene is a 2D crystal consisting of one layer of carbon atoms which are arranged in a hexagonal lattice [10], as shown in Figure 2.2.A. Graphene was firstly isolated from graphite by mechanical exfoliation [2] and has been an important material base for the van der Waals heterostructures [1].

The electronic properties of graphene were reviewed in detail in Reference [10]. The graphene lattice structure results in a hexagonal Brillouin zone, which is shown Figure 2.2.B. The unique electronic properties of graphene come from its band structure. The conduction and valence band touches only at the corners of the Brillouin zone (K and K' point), as shown in Figures 2.2, C and D. The touching points are called Dirac points, resulting in the Dirac cones which holds linear dispersion relationship in the vicinity of the Dirac points [10]. This electronic

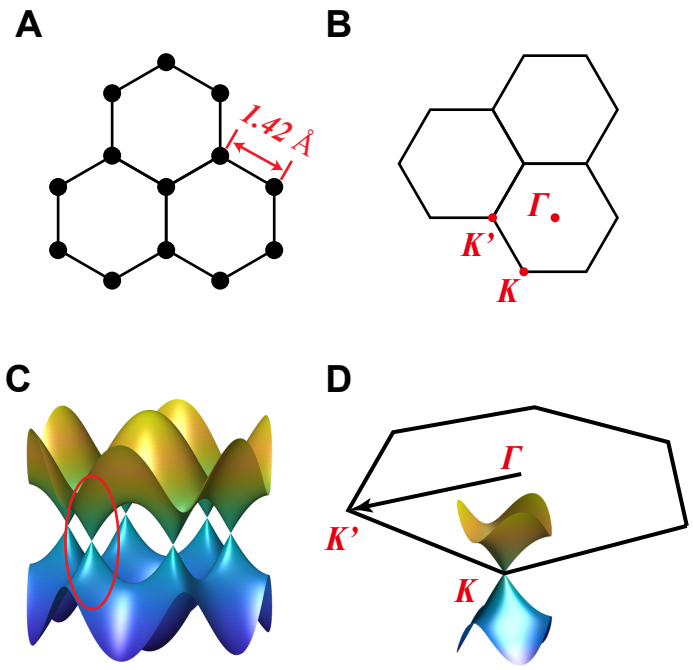

Figure 2.2: Graphene band structure. A. Crystal structure of graphene. The black dots show the arrangement of carbon atoms. **B.** Brillouin zones of graphene. **C.** Graphene band structure. **D.** Zoom-in of the graphene band structure at K point.

structure causes the electrons in graphene act as massless particles and follow the massless Dirac equations [2]. In an electrically neutral graphene, the Fermi surface stays at the Dirac points [10]. However, the Fermi surface often shifts when the graphene is on top of a substrate [11]. In Section 2.3, we will look into this doping effect when multiple layers of graphene are stacked together on top of a copper substrate.

2.2 Layer number dependence of photoemission intensity

As illustrated in Figure 2.3, the beam spot is focused to scan over the sample in a micro-ARPES measurement. In the few-layer graphene system on copper substrate, the intensity of photoelectrons which are from the substrate and collected when the beam spot is on different parts of the sample can be used to produce the contrast for domains with different layer numbers.

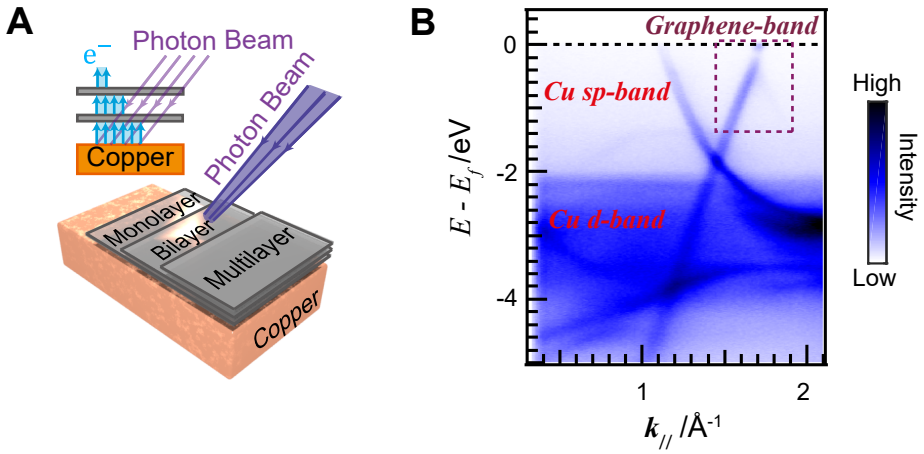

Figure 2.3: D-band from the copper substrate. A. Illustration of micro-ARPES spatial scanning of multilayer graphene on copper foil substrate. The inset shows the absorption of photoelectrons from the copper by consecutive graphene layers. **B.** An energy-momentum dispersion map showing bands from graphene on copper substrate.

The absorption of the photoelectrons from the substrate by each layer provides the contrast in the real-space scan in in areas with different layer numbers. For the copper substrate, the flat copper d-band shown in Figure 2.3.B stays at the binding energy $E - E_F = -2\,\text{eV}$ to $-4\,\text{eV}$. By setting the analyser energy window to this range and scanning the photon beam through the sample surface, an intensity map is produced in Figure 2.4.A, revealing clear contrast on 1-5 layers of graphene across the sample. This contrast is the result of integrating the intensity data through the k dimension and E dimension for each position.

To check the difference of the electronic structure in each domains, we extract the Energy Distribution Curves (EDC) from 5 typical positions with layer number 1 to 5 and present them in Figure 2.4.B. Indeed, the peak intensity from the copper d-band at the energy window from $E - E_F = -2\,\text{eV}$ to $-4\,\text{eV}$ decreases with increasing layer number.

To determine the penetration depth of the photoelectrons in the graphene layers, a more quantitative analysis of the integrated photoelectron intensity is shown in Figure 2.4.C. The decay of the integrated intensity with the increasing number of the overlaying graphene layers presents an exponential trend. The fitting to the curve with a simple model $I = I_0 e^{-x/\lambda} + I_1$ (x is the layer number and I_0 and

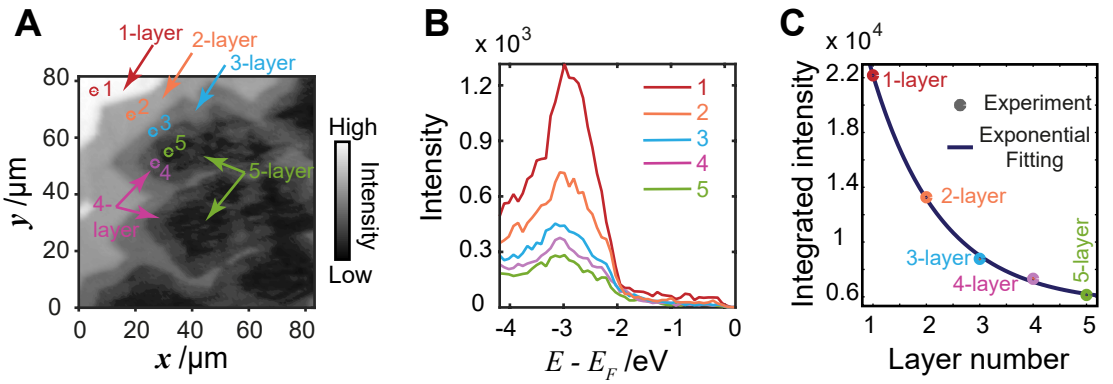

Figure 2.4: Micro-ARPES real space scan. A. Large-scale spatial scanning image of the sample in the spectral range of the copper d-bands. Dots with different color mark selected positions for subsequent measurement. The lighter color shows higher intensity of the integrated spectrum. **B.** Energy Distribution Curves (EDCs) from the positions in domains with different layer numbers, marked with the dot of the corresponding color in B. **C.** Integrated intensity from the corresponding EDCs in C, plotted over layer number, and exponential fitting curve (dark blue line).

I_1 are fitting constants) yields that the average photoelectron penetration depth is $\lambda = 1.3 \pm 0.3$ graphene layers, i.e. the absorption rate is $54\% \pm 9\%$ per layer, indicating that micro-ARPES is capable of the study of multilayer graphene up to 5 layers with 5% intensity from the bottom layer.

In the above analysis, the photon beam attenuation across the layers is ignored. This is due to the penetration depth of the photon beam is relatively large compared to the thickness of each graphene layer (∼3.3 Å) [12].

Another technical discussion is in the data recording format for the real-space scan. Ideally, an energy-momentum dispersion map is recorded for each of the positions, resulting in a four-dimensional data set (k-E-X-Y). However, due to the time limit for an ARPES experiment, the exposure time for each map is very limited. Assuming the spatial step is 1 µm for an 80-by-80 µm^2 area, there are 6400 points in total for the spatial scan. For a half-hour mapping, the exposure time for each point should be about 0.3 second, resulting in very low data quality. Due to this time limit and the data-dimension restriction, the common data representation is to integrate the energy-momentum dispersion map within a certain energy window and then plot against the real-space coordinates. The contrast of the integrated real-space map represents different sample domains. To characterize the electronic structure

of the region of interest, subsequent detailed experiments can be performed with the guidance of this real-space map.

To conclude, this domain-resolving capability enables us to visualise the sample morphology, to identify the region of interest and to compare the electronic structure from different locations.

2.3 Substrate doping effect in few-layer system

Exploiting the capability to identify graphene domains with different thicknesses, we directly observe the substrate doping effect on multilayer graphene: with increasing number of layers, the top layer of graphene becomes less electron-doped. The doping effect for a monolayer thin film on the metallic substrate was theoretically discussed in Reference [13] by using an effective capacitor model: considering an effective chemical potential between the monolayer and the substrate and modelling the electron transfer as in a capacitor. In this section, we report the experimental observation of the substrate doping effect in a multilayer system with metal substrate and explain this effect by extending the effective capacitor model from a monolayer system to a multilayer system, which fits the experiment data.

2.3.1 Observing the substrate doping effect

We staged the analyser at the same angle for the K point of the graphene Brillouin zone (BZ) and focused the photon beam position at the points No.1 to No.5 in Figure 2.5.A to measure the energy-momentum intensity map for the five positions consecutively. As can be seen in Figure 2.5.B, the doping level of the graphene band rises from $-0.53\,\mathrm{eV}$ for the one-layer domain to $-0.13\,\mathrm{eV}$ for the five-layer domain as shown in Figure 2.5.C.

We argue that the band seen here is from the top layer, which is the same large single crystal graphene layer, for all the five domains. The reasons for this arguments are: A. The CVD grown few-layer graphene tends to have an 'inverse pyramid' layer arrangement so the topmost layer is larger than the underlying layers (see Reference [14] and the discussion in Section 3.4). and B. The angle of the

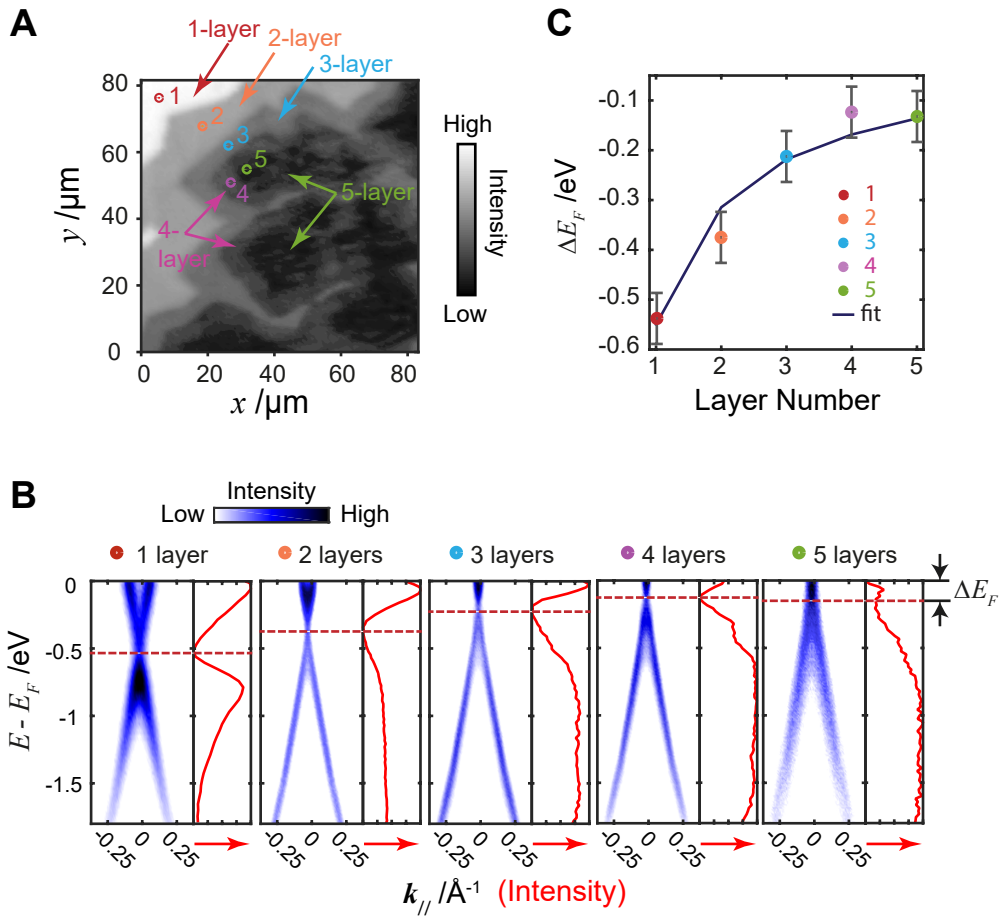

Figure 2.5: Energy momentum dispersion map at different sample domains. **A.** The same large-scale spatial scanning image of the sample as in Figure 2.4.A. Dots with different color mark selected positions for subsequent measurement. The lighter color shows higher intensity of the integrated spectrum. **B.** Energy-momentum-dispersions taken at positions shown in A. Red dashed lines indicate the energy of the Dirac point (E_D) in each spectrum of the top layer. The changing of the Fermi energy is defined as $\Delta E_F = E_D - E_F$. Red solid curves are integrated EDCs for each spectrum, which are corrected by the Fermi-Dirac distribution, allowing to see features near the Fermi Surface. **C.** Evolution of ΔE_F of the top layer with total number of layers. The dark blue line indicates a fit of the data using the effective capacitor model described in Section 2.3.

analyser is the same throughout the five measurements and the K point does not change position at all, suggesting the crystal orientation is homogeneous [15].

To explain the rise of the Fermi level with decreasing layer number, we extend the effective capacitor model that describes a monolayer film covering on a metallic substrate to a multilayer system.

2.3.2 Effective capacitor model for monolayer system

The single layer effective capacitor model is illustrated in Figure 2.6.A. Due to the work function difference between the metal substrate (W_{Cu}, copper in our case) and the graphene layer (W_G), as well as considering an effective work function W_{Chem} caused by chemical interactions, electrons will be transferred from the substrate to the graphene layer, filling the originally unoccupied states and forming an electric field with electric potential U between the substrate and the graphene layer (as shown in Figure 2.6.B). As a result, the binding energy of the Dirac cone will increase by an energy ΔE_F. In the equilibrium state, the following equation will hold:

$$W_{Cu} + eU + W_{Chem} = W_G + \Delta E_F \tag{2.1}$$

where

$$U = \sigma d/\epsilon_0 \tag{2.2}$$

σ is the charge transferred per unit area, ϵ_0 is the electric constant, and d is the effective distance defined in Reference [14], which is smaller than the real distance between the substrate and the graphene layer due to the attraction between positive and negative charge clouds.

To analyse the relationship between transferred electron density σ and binding energy shift ΔE_F, we start with the density of state (DOS) of graphene near the Dirac point, which is

$$D(E) = D_0 E$$

with $D_0 = 0.09$ per (eV^2) per unit cell [13]. The number of electrons transferred to each unit cell is given by integrating the DOS between $E = 0$ and $E = \Delta E_F$, which is

$$N = \frac{D_0}{2}\Delta E_F^2$$

The charge density is then given by

$$\sigma = \frac{eN}{A} = \frac{eD_0}{2A}\Delta E_F^2$$

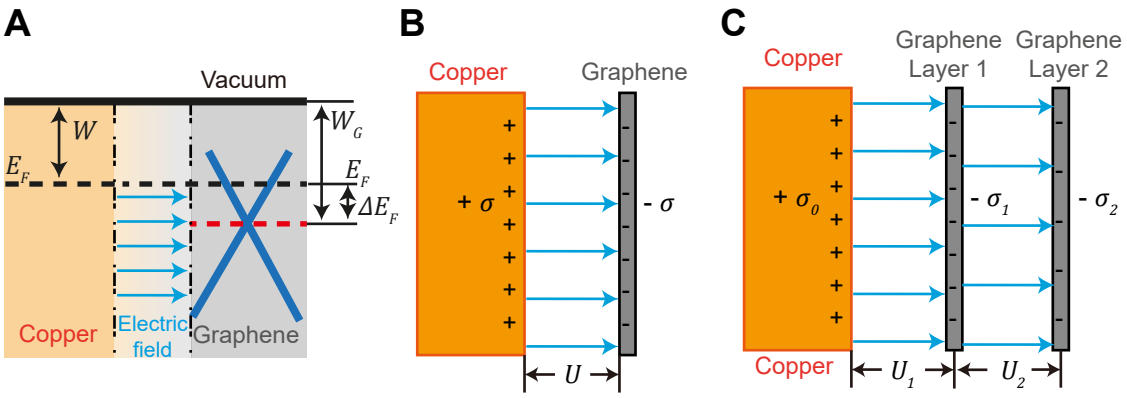

Figure 2.6: Effective capacitor model for multilayer doping effect. A. Illustration for the effective capacitor model. Due to the charge transfer, there is an electric field between copper substrate and graphene layer, which leads to a shift ΔE_F of the Dirac cone to higher binding energies. W_G is the work function of free standing graphene, and W the work function of the whole system. **B.** The simplified illustration of the model for the one-layer case. $\pm\sigma$ is the transferred charge per unit area, and U the electric potential. **C.** Illustration of the model for the two-layer case. σ_i is the transferred charge per unit area for the i-th-layer.

Where A is the area of a graphene unit cell. Thus, we can get U from Equation 2.2

$$U = \frac{eD_0 d}{2A\epsilon_0}\Delta E_F^2$$

Using the expression of U above, we can rewrite Equation 2.1 as

$$\frac{e^2 D_0 d}{2A\epsilon_0}\Delta E_F^2 - \Delta E_F + W_{Chem} + W_{Cu} - W_G = 0$$

or

$$\alpha \cdot \Delta E_F^2 - \Delta E_F + W_{eff} = 0 \tag{2.3}$$

where

$$\alpha = \frac{e^2 D_0 d}{2A\epsilon_0}$$

We can solve Equation 2.3 for ΔE_F in terms of α and W_{eff}.

2.3.3 Extend the effective capacitor model to multilayer system

We extend this effective capacitor model to the multilayer system to explain the experiment data.

In the following discussions, the subscripts in U_{ij} and ΔE_{Fij} i and j denotes for the j-th layer's quantity in an i-layer system. The i-th layer in a i-layer system is the topmost layer, which is the furthest one from the substrate.

We can rewrite the equation for the monolayer system:

$$\alpha \cdot \Delta E_{F11}^2 - \Delta E_{F11} + W_{eff} = 0 \tag{2.4}$$

For the two layer system in Figure 2.6.C, the electrons will be transferred to graphene layer 1 and layer 2 to reach static electronic equilibrium. The charge density in layer 1 is $-\sigma_1$ while the charge density in layer 2 is $-\sigma_2$, and the charge density in the metal substrate is $\sigma_0 = \sigma_1 + \sigma_2$.

The electronic field U_1 exists between layer 1 and the substrate while U_2 exists between layer 2 and layer 1.

We can now formulate equations for this stacked two-layer system.

For the substrate we have

$$W = W_{Cu} + eU_{21} + W_{Chem} + eU_{22} \tag{2.5}$$

For the first layer

$$W = W_G + \Delta E_{F21} + eU_{22}, \tag{2.6}$$

and for the second layer (the top layer):

$$W = W_G + \Delta E_{F22} \tag{2.7}$$

Similar to the monolayer case, we have

$$\sigma_{ij} = \frac{eD_0}{2A} \Delta E_{Fij}^2,$$

which allows us to solve Equations 2.5 and 2.6:

$$U_{21} = \frac{\sigma_{21} d}{\epsilon_0} + \frac{\sigma_{22} d}{\epsilon_0} = \frac{eD_0 d}{2A\epsilon_0} \left(\Delta E_{F21}^2 + \Delta E_{F22}^2 \right) = \frac{\alpha}{e} \left(\Delta E_{F21}^2 + \Delta E_{F22}^2 \right)$$

$$U_{22} = \frac{\sigma_2 d}{\epsilon_0} = \frac{\alpha}{e} \Delta E_{F22}^2$$

Thus, we can rewrite Equations 2.5, 2.6 and 2.7

$$\begin{cases} \alpha\left(\Delta E_{F21}^2 + \Delta E_{F22}^2\right) - \Delta E_{F21} + W_{eff} = 0 \\ \alpha\Delta E_{F22}^2 - \Delta E_{F22} + \Delta E_{F21} = 0 \end{cases} \tag{2.8}$$

By solving this system of coupled equations, we can write ΔE_{F22} in a functional form with the variables α and W_{eff}:

$$\Delta E_{F22} = F_2(\alpha, W_{eff})$$

in which α and W_{eff} are the same parameters in the monolayer system. We also assume that E_{F22} is a negative number, which means the binding energy for the Dirac point is negative.

By extending this model up to 5-layer systems, we could solve the euqation system for each one, and use these equations to fit the two parameters, α and W_{eff}.

Specifically, for the three-layer system

$$\begin{cases} \alpha\left(\Delta E_{F31}^2 + \Delta E_{F32}^2 + \Delta E_{F33}^2\right) - \Delta E_{F31} + W_{eff} = 0 \\ \alpha\Delta E_{F32}^2 - \Delta E_{F32} + \Delta E_{F31} = 0 \\ \alpha\Delta E_{F33}^2 - \Delta E_{F33} + \Delta E_{F32} = 0 \end{cases} \tag{2.9}$$

And we have $\Delta E_{F33} = F_3(\alpha, W_{eff})$.

For the four-layer system

$$\begin{cases} \alpha\left(\Delta E_{F41}^2 + \Delta E_{F42}^2 + \Delta E_{F43}^2 + \Delta E_{F44}^2\right) - \Delta E_{F41} + W_{eff} = 0 \\ \alpha\Delta E_{F42}^2 - \Delta E_{F42} + \Delta E_{F41} = 0 \\ \alpha\Delta E_{F43}^2 - \Delta E_{F43} + \Delta E_{F42} = 0 \\ \alpha\Delta E_{F45}^2 - \Delta E_{F44} + \Delta E_{F43} = 0 \end{cases} \tag{2.10}$$

And we have $\Delta E_{F44} = F_4(\alpha, W_{eff})$.

For the five-layer system

$$\begin{cases} \alpha\left(\Delta E_{F51}^2 + \Delta E_{F52}^2 + \Delta E_{F53}^2 + \Delta E_{F54}^2 + \Delta E_{F55}^2\right) - \Delta E_{F51} + W_{eff} = 0 \\ \alpha\Delta E_{F52}^2 - \Delta E_{F52} + \Delta E_{F51} = 0 \\ \alpha\Delta E_{F53}^2 - \Delta E_{F53} + \Delta E_{F52} = 0 \\ \alpha\Delta E_{F54}^2 - \Delta E_{F54} + \Delta E_{F53} = 0 \\ \alpha\Delta E_{F55}^2 - \Delta E_{F55} + \Delta E_{F54} = 0 \end{cases} \tag{2.11}$$

Fermi level shift	Experiment ΔE^{ob}_{Fii}	Fitting ΔE^{*}_{Fii}
ΔE_{F11}	$-0.53\,\mathrm{eV}$	$-0.55\,\mathrm{eV}$
ΔE_{F22}	$-0.37\,\mathrm{eV}$	$-0.31\,\mathrm{eV}$
ΔE_{F33}	$-0.21\,\mathrm{eV}$	$-0.22\,\mathrm{eV}$
ΔE_{F44}	$-0.12\,\mathrm{eV}$	$-0.17\,\mathrm{eV}$
ΔE_{F55}	$-0.13\,\mathrm{eV}$	$-0.14\,\mathrm{eV}$

Table 2.1: Fitting result of the experimental Fermi level shift. ΔE_{Fij} stands for the Fermi level shift of the j-th graphene layer in an i-layer system. ΔE_{Fii} is for the topmost layer. The fitted parameters are $\alpha = 1.80\,\mathrm{eV}^{-1}$ and $W_{eff} = -1.09\,\mathrm{eV}$. Residual sum of squares is $0.006\,\mathrm{eV}^2$.

And we have $\Delta E_{F55} = F_5(\alpha, W_{eff})$.

The experimental observables are $E_{Fii}, i = 1, 2, 3, 4, 5$.

In the ARPES measurement, we conclude ΔE_{F11}, ΔE_{F22}, ΔE_{F33}, ΔE_{F44} and ΔE_{F55} in Table 2.1, and we are able to fit these two parameters from the five data points.

Noting that we cannot write down $F_i(\alpha, W_{eff})$ analytically, we could still fit the data points using numerical methods. We can define a loss function $\mathscr{L}$ by using the sum of residual between the experiment results (ΔE^{ob}_{Fii}) and the fitted result $F_i(\alpha, W_{eff})$:

$$\mathscr{L} = \sum_{i=1}^{5} (\Delta E^{ob}_{Fii} - F_i(\alpha, W_{eff}))^2$$

and then calculate and minimize $\mathscr{L}$ numerically with respect to α and W_{eff}.

The fitting result is presented in Figure 2.5.C, with $\alpha^{fit} = 1.80\,\mathrm{eV}^{-1}$ and $W^{fit}_{eff} = -1.09\,\mathrm{eV}$. The fitting result shows good agreement with the experiment, with the residual sum of squares $0.006\,\mathrm{eV}^2$.

2.4 Discussion and conclusion

We note that the electrons from lower graphene layers are not found in Figure 2.5.B as they are either too weak or outside the detection window. But in some domains of twisted bi- and multilayer graphene we could detect multiple Dirac cones from each layer, which allow us to observe the electronic structure where the Dirac cones are intersecting, as discussed in Chapter 3.

To conclude, we have demonstrated that micro-ARPES has the sample morphology mapping ability using the intensity contrast from the different sample positions. We discussed that in a multilayer graphene system, the absorption rate from each covering layer for the photoelectrons is about 54%, resulting in a 5% intensity for the substrate electrons in a five-layer system. Using this real-space scanning ability, we locate the region of interest and further study the electronic structures in different sample domains. We report a substrate doping effect and explain the layer-dependence of the doping effect using an effective capacitor model. These systematic results can be used as a reference in future micro-ARPES studies in multilayer systems.

Bibliography

[1] Andre K Geim and Irina V Grigorieva. "Van der Waals heterostructures". In: *Nature* 499.7459 (2013), p. 419.

[2] KSA Novoselov et al. "Two-dimensional gas of massless Dirac fermions in graphene". In: *Nature* 438.7065 (2005), pp. 197–200.

[3] Yuanbo Zhang et al. "Experimental observation of the quantum Hall effect and Berry's phase in graphene". In: *Nature* 438.7065 (2005), pp. 201–204.

[4] F. Xia et al. "Ultrafast graphene photodetector". In: *Nature Nanotechnology* 4.12 (2009), pp. 839–43. URL: `http://www.ncbi.nlm.nih.gov/pubmed/19893532`.

[5] Konstantin S Novoselov et al. "A roadmap for graphene". In: *Nature* 490.7419 (2012), p. 192.

[6] M. Sprinkle et al. "First Direct Observation of a Nearly Ideal Graphene Band Structure". In: *Physical Review Letters* 103.22 (2009).

[7] SK Mahatha, KD Patel, and Krishnakumar SR Menon. "Electronic structure investigation of MoS_2 and $MoSe_2$ using angle-resolved photoemission spectroscopy and ab initio band structure studies". In: *Journal of Physics: Condensed Matter* 24.47 (2012), p. 475504.

[8] Pavel Dudin et al. "Angle-resolved photoemission spectroscopy and imaging with a submicrometre probe at the SPECTROMICROSCOPY-3.2 L beamline of Elettra". In: *Journal of Synchrotron Radiation* 17.4 (2010), pp. 445–450.

[9] Jose Avila et al. "ANTARES, a scanning photoemission microscopy beamline at SOLEIL". In: *Journal of Physics: Conference Series* 425.19 (2013), p. 192023.

[10] A. H. Castro Neto et al. "The electronic properties of graphene". In: *Reviews of Modern Physics* 81.1 (2009), pp. 109–162.

[11] S. Y. Zhou et al. "Substrate-induced bandgap opening in epitaxial graphene". In: *Nature Materials* 6.10 (2007), pp. 770–5. URL: `http://www.ncbi.nlm.nih.gov/pubmed/17828279`.

[12] MP Seah and WA Dench. "Quantitative electron spectroscopy of surfaces: a standard data base for electron inelastic mean free paths in solids". In: *Surface and Interface Analysis* 1.1 (1979), pp. 2–11.

[13] G. Giovannetti et al. "Doping Graphene with Metal Contacts". In: *Physical Review Letters* 101.2 (2008).

[14] Shu Nie et al. "Growth from below: bilayer graphene on copper by chemical vapor deposition". In: *New Journal of Physics* 14.9 (2012), p. 093028.

[15] HF Yang et al. "Single crystalline electronic structure and growth mechanism of aligned square graphene sheets". In: *APL Materials* 6.3 (2018), p. 036107.

3

Band structure of twisted few-layer graphene

Contents

After introducing the micro-ARPES' ability to differentiate different domains on the substrate, we now focus on the bilayer and trilayer graphene domains with twist angle between the layers. In this chapter, we systematically study the twist angle evolution of the energy band of twisted few-layer graphene over a wide range of twist angles (from 5° to 31°). We directly observe van Hove Singularities (vHSs) in twisted bilayer graphene with wide tunable energy range over 2 eV. In addition, the formation of multiple vHSs (at different binding energies) is observed in trilayer

graphene. The large tuning range of vHS binding energy in twisted few-layer graphene provides a promising material base for optoelectrical applications with broad-band wavelength selectivity.

3.1 Introduction to twisted bilayer graphene

Graphene exhibits unusual electronic structures and physical properties[1–3] that make it attractive for high-performance devices, such as transistors[4–7], optical modulators[8, 9] and photodetectors [8, 10]. Compared to single layer graphene, when two or more layers of graphene are stacked together with a twist angle, their electronic structure can be further enriched, giving rise to the van Hove singularity (vHS) with greatly enhanced carrier density of states, thus leading to enhanced optical absorption for selective photon energies [11–16]. With large tuning range of the twist angle and vHS binding energy, twisted bi- and multilayer graphene provide a promising material base for fabricating broad band wavelength-selective ultrafast photodetectors from the infrared to the ultraviolet regime.

However, despite the consensus about the existence of vHSs for small twist angles ($\leqslant 5°$) [16–21], the formation of vHS for large twist angles is still under debate. Although scanning tunneling microscopy (STM) studies found that two layers with larger twist angle (5.5° in Reference [20] and 20° in Reference [21], respectively) decouple and the electronic structure becomes indistinguishable from monolayer graphene, recent optical and theoretical studies suggest that the vHSs may persist at large twist angles up to 30° [17, 18, 22–24]. To settle this discrepancy, it is required to systematically and directly investigate the electronic structure of twisted bi- and multilayer graphene over a wide twist angle regime.

As discussed in Chapter 2, the recent development of micro-ARPES provides an excellent tool to obtaining complete electronic structures of samples down to 1 µm, allowing us to investigate and to compare graphene domains with varying twist angles.

In this work, we apply the micro-ARPES to study the twisted few-layer graphene sheets. We observe the van Hove singularity (vHS) directly in twisted bi- and trilayer graphene and find the evidence of super-potential modulation in the twisted

bilayer graphene electronic structure. We then systematically study the twist angle evolution of vHS in the twisted bi- and trilayer graphene. We observe not only the vHSs in twisted bilayer graphene (tBLG) over a wide range of twist angle (from 5° to 31°), but also co-existence of multiple vHSs at different energies in twisted trilayer graphene (tTGL). Our result suggests that the inter-layer coupling persists at large twist angles. This discovery allows one to tune the binding energy of the vHS up to over 2 eV, thus leading to a promising application in wavelength-selective ultrafast photodetection from infrared to ultraviolet regime. We demonstrate this application by a proof-of-principle photodetector with a much enhanced photocurrent generation at the photon energy that matches the binding energy of the vHS.

3.2 Band structure of twisted bilayer graphene

3.2.1 Region selection using micro-ARPES

Using the spatial resolution of micro-ARPES discussed in 2.2, we can directly compare the optical image and the real-space scan image. An optical microscope image (Figure 3.1.A) and the spatially ARPES scanning (Figure 3.1.B) clearly show the graphene domains on the Cu substrate. Especially, the spatially ARPES scanning results show much better contrast that enables us to differentiate the layer number in the graphene domains, which allows the further identification of the region of the interest. By taking finer steps, the images with larger zoom-in scale (Figures 3.1, C and D) reveal more details of the sample morphology. As shown in Figure 3.1.D, we can identify the monolayer, bilayer and trilayer graphene in a small sample region. By looking at the alignment of the edges of different layers, we can already see that layer 1 and layer 2 are twisted. The subsequent micro-ARPES electronic structure measurement in position P1 and P2 will further confirm the twist.

3.2.2 Van Hove Singularity in the twisted bilayer band structure

The measurement of the electronic structure at point P1 from Figure 3.1.D shows a typical band dispersion of twisted bilayer graphene in Figure 3.2, which displays

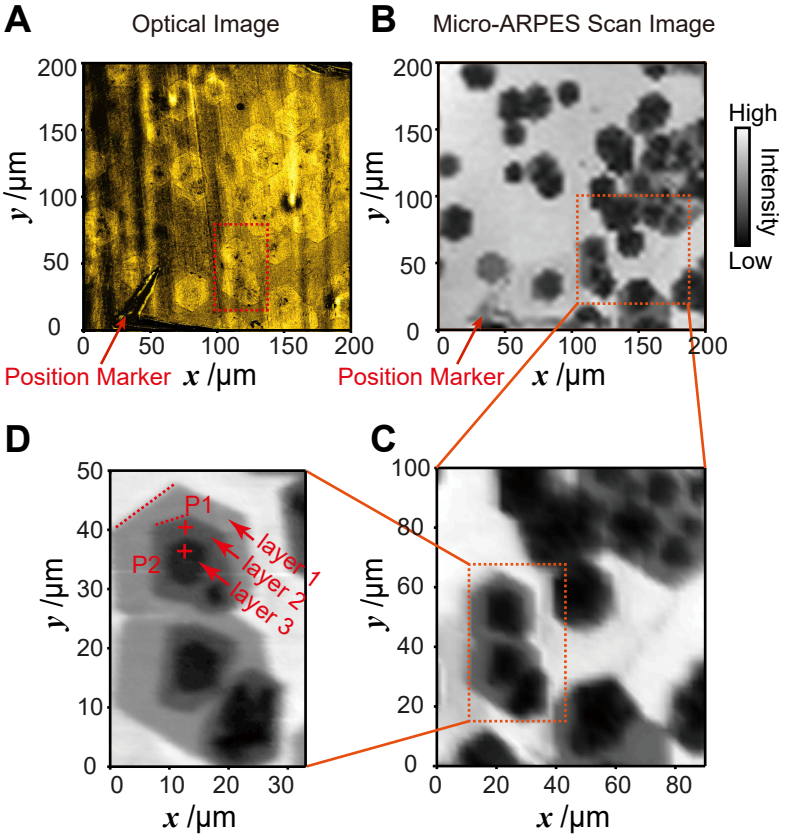

Figure 3.1: Region selection of twisted multilayer graphene. A. Optical microscope image of the bilayer graphene sample to identify the region of interest. The red square indicates where the subsequent micro-ARPES fine scanning were taken. **B-D.** Spatial scanning images of the region of interest with increasing magnification. To achieve higher resolution, finer scanning steps were adopted. The red crosses in D show the two positions where the micro-ARPES band structure measurements are taken. The red arrows mark the regions with different number of graphene layers (from monolayer to trilayer).

two Dirac cones shifted in momentum space due to a twist angle. To understand this electronic structure, consider the illustration shown in Figures 3.2, A and B. In a bilayer graphene system, the bottom layer crystal rotates by an angle θ relative to the top layer. The Brillouin zone (BZ) will rotate accordingly with the bottom layer lattice, making the $\boldsymbol{K}_\theta$ point shifts away from the original $\boldsymbol{K}$ point. From simple geometry, the distance between $\boldsymbol{K}_\theta$ and $\boldsymbol{K}$ points, $\Delta k = 2|\boldsymbol{K}| \sin\theta/2$.

By measuring the exact shift Δk between the two cones, we find the twist angle is 8.2°. We can even tell in Figure 3.2.C that the Dirac cone marked with **K** is

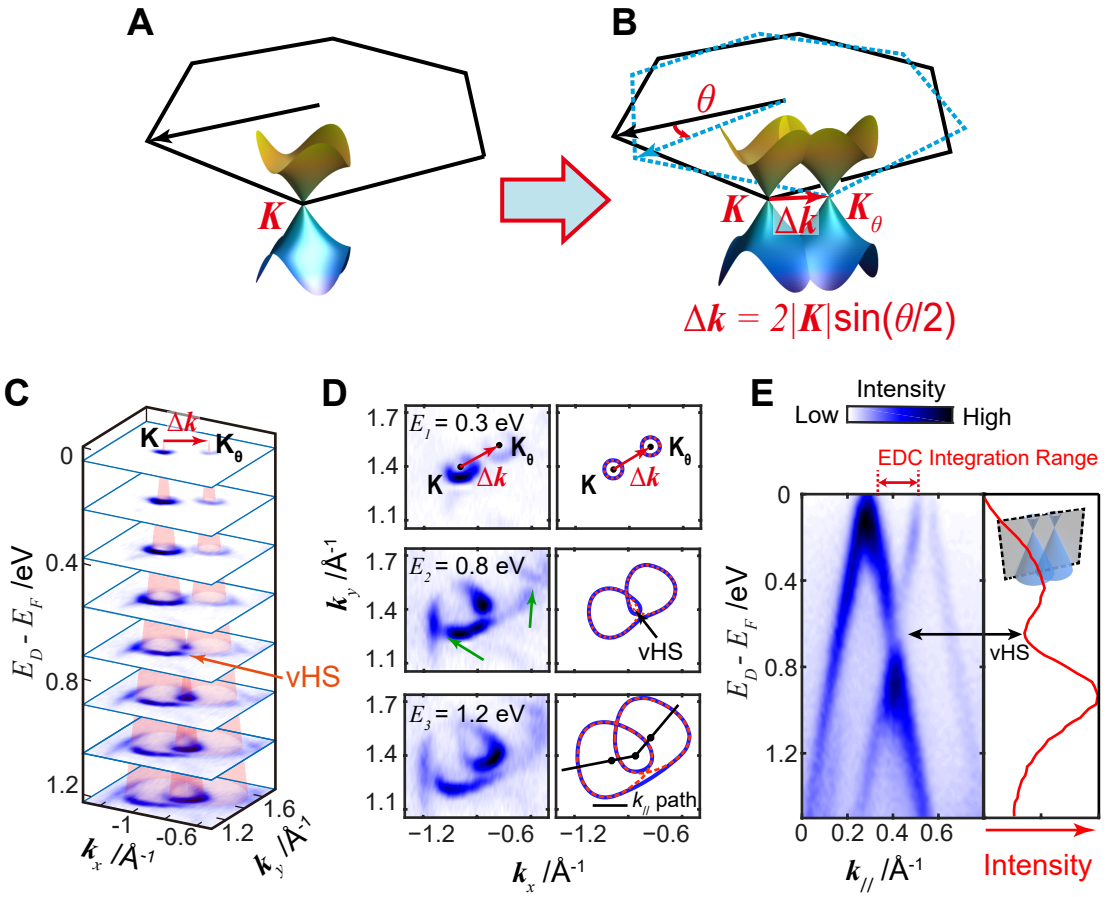

Figure 3.2: Band structure of twisted bilayer graphene. **A.** Illustration of Brillouin Zone (BZ) and the band structure near $\boldsymbol{K}$ point for the monolayer graphene. **B.** Illustration of Brillouin Zone (BZ) and the band structure near $\boldsymbol{K}$ point for the twisted bilayer graphene (tBLG). As one graphene layer rotates for an angle of θ relative to the other, the BZ will also rotate for the θ angle accordingly. The red arrow marks the vector $\Delta\boldsymbol{k}$, which is the difference between the original $\boldsymbol{K}$ point in the BZ and its rotated counterpart, $\boldsymbol{K}_\theta$ point. **C.** Equal energy contours of tBLG band structure with twist angle 8.2° measured at P1 from Figure 3.1.D, showing two Dirac cones. **D.** Comparison between measured and illustrating energy contours. The dotted red curves are calculated from a tight binding model for the overlapping bands from two Dirac cones without considering the inter-layer hybridization. The solid blue curves are a guide to the eye to illustrate the hybridization effect. The mini gaps marked by green arrows stem from a Moiré superpotential, which is presented with more details in Figure 3.3. **E.** Energy-momentum dispersion map measured at P1 passing through the two Dirac points and the van Hove singularity ($k_{\parallel}$ path is indicated in the bottom of B. The right panel shows the integrated EDC over the region shown above.

from the top layer and the Dirac cone marked with $\mathbf{K}_\theta$ is from the lower layer, since the spectrum of Dirac cone from the lower layer is weaker due to the depth attenuation effect discussed in Chapter 2.

When the two Dirac cones intersect, they hybridize and open up a gap, forming the vHS at the saddle point, which can be seen both in the constant energy band contours (Figure 3.2.D) and the energy-momentum dispersion map (Figure 3.2.E). From the dispersions and the corresponding integrated energy distribution curve (EDC), we can also see that the vHS provides a large density of states near the gap (Figure 3.2.E). In addition to the gap opened at the crossing point, mini gaps are observed in the equal energy contours (green arrows in the middle panel) due to a Moiré superpotential (see more discussions in Section 3.2.3).

3.2.3 Mini Brillouin zone of the twisted bilayer

In the equal energy surfaces of band structure of tBLG in Figure 3.2, we can observe the opening of two gaps in the Dirac cones. The one highlighted by the red arrow in Figure 3.3 is at the crossing point of the two original cones from the two twisted layers. However, an additional gap opening, highlighted by the black arrow in the same Figure, cannot be explained by the crossing of the two original cones. This unusual gap is also reported in Reference [15] and is explained by a superpotential generated by the disorientation of two graphene layers, which leads to a mini Brillouin zone (mini BZ) that is shown by the black dotted lines in Figure 3.3.B. Ohta et al. speculate the presence of additional Dirac cones at corners of the mini BZ, and report its weak signature in a second derivative plot of their data. Here, we give for the first time direct evidence for the existence of Dirac cone replica in twisted bilayer graphene.

In Figure 3.3.B, the $\mathbf{K}$ point of the top-layer BZ is indicated by a red dot that marks the centre of the top layer Dirac cone. The extent of this cone is indicated by the red circle. The blue dot at $\mathbf{K}_S$ marks the suspected centre of the additional Dirac cone at the corner of one mini BZ, with its suspected extend indicated by the blue circle. To prove the existence of this additional Dirac cone at $\mathbf{K}_S$, a detailed

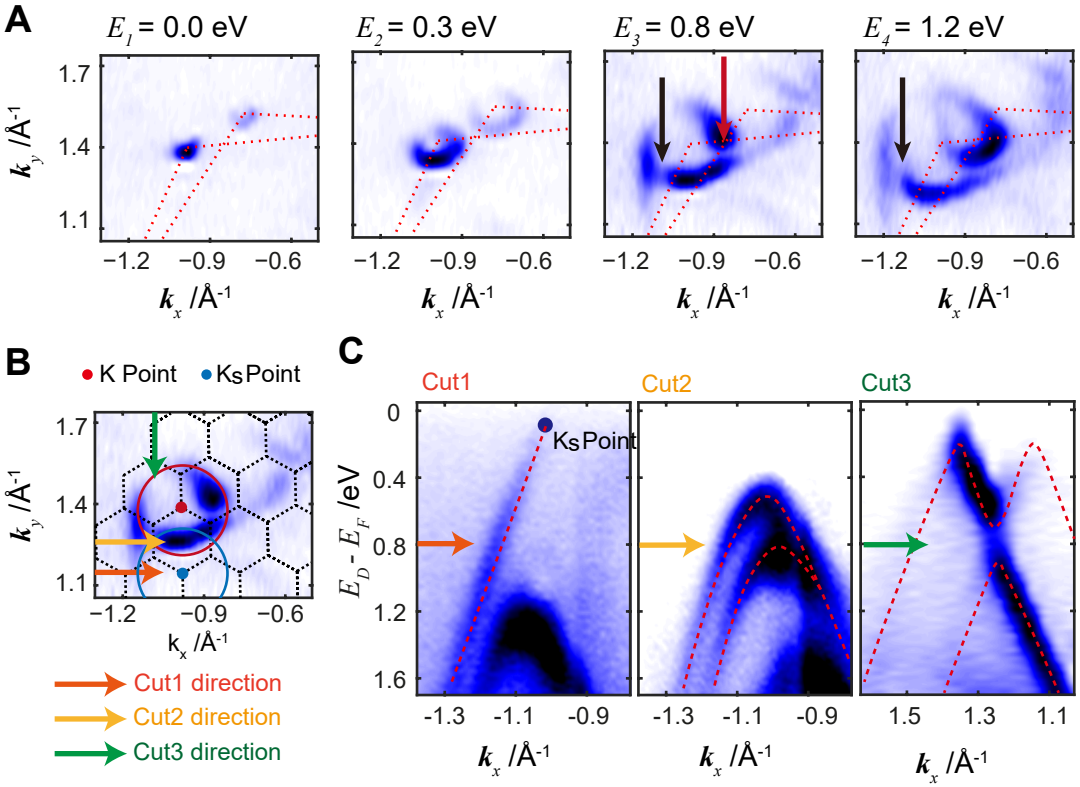

Figure 3.3: Mini Brillouin zone in tBLG band structure and emergence of superpotential cone. A. Equal energy surfaces of tBLG band structure. The red dotted line indicates the hexagonal shape of two twisted single-layer Brillouin zones. The red arrow shows the position of vHS and the black arrows show the position of an additional gap that cannot be explained by the crossing of the two original cones. **B.** Equal energy surface at 0.8 eV binding energy. The K point from the top layer is marked by a red dot and the Dirac cone is indicated by a red circle. The K_s point is marked by a blue dot and the additional Dirac cone generated by the superpotential is indicated by the blue circle, while the black dotted line indicates the corresponding mini Brillouin zone. **C.** Band structure of the additional superpotential Dirac cone. Cut1 (along the orange arrow in B) shows the linear dispersion in the vicinity of its centre K_s. Cut2 (along the yellow arrow in B) shows its hyperbolic dispersion off-centre. Cut3 (along the green arrow in B) shows a perpendicular cut through the additional vHS at the crossing point between the top layer cone and the superpotential cone, which leads to one M-shaped and one Λ-shaped band.

analysis in Figure 3.3.C presents two cuts along the directions marked by the orange and yellow lines in Figure 3.3.B. The first cut through $\mathbf{K}_S$ (direction indicated by an orange arrow) shows a linear dispersion which is attributed to the additional cone. The weakness of the signal in the right arm might be caused by the matrix element. The second cut through the crossing points of the two cones (direction indicated by a yellow line) shows the hyperbolic signature of the cone at $\mathbf{K}_S$ and thereby gives conclusive evidence for its existence.

After identifying an additional Dirac cone, we now can further infer that the additional gap, indicated by the black arrow in Figure 3.3.A, is generated by the crossing and hybridization of the red and blue Dirac cones centred the **K**-point and $\mathbf{K}_S$-point. To verify this, Figure 3.3.C shows a third cut through the crossing point of the cones that is perpendicular to the previous ones, whose direction is indicated by the green arrow in Figure 3.3.B. We identify an M-shaped band and an Λ-shaped band, which is highlighted by the red dashed line. A gap is opened between the two bands, which lies at the crossing point of two Dirac cones, showing that an additional van Hove Singularity is formed.

3.3 Twist angle dependence of twisted bilayer graphene band structure

3.3.1 Evolution of binding energy of van Hove Singularity

We now focus on the bilayer graphene domains and investigate the relationship between the twist angle and the binding energy of vHSs, a collection of energy-momentum dispersion maps from the twisted bilayer graphene are shown in Figure 3.4, with twist angle ranging from 5° to 31°. The evolution of the vHS binding energy can be well reproduced by a theoretical model (Figure 3.5.A) [22]: the binding energy of vHS depends on the position of the intersection between the two Dirac cones from different layers. As the the twist angle increases, the separation between the two cones, Δk, also increases. This will result in a larger binding energy for the intersection position. Considering a tight binding calculation for the single layer energy band and the intersection with the same band but with a

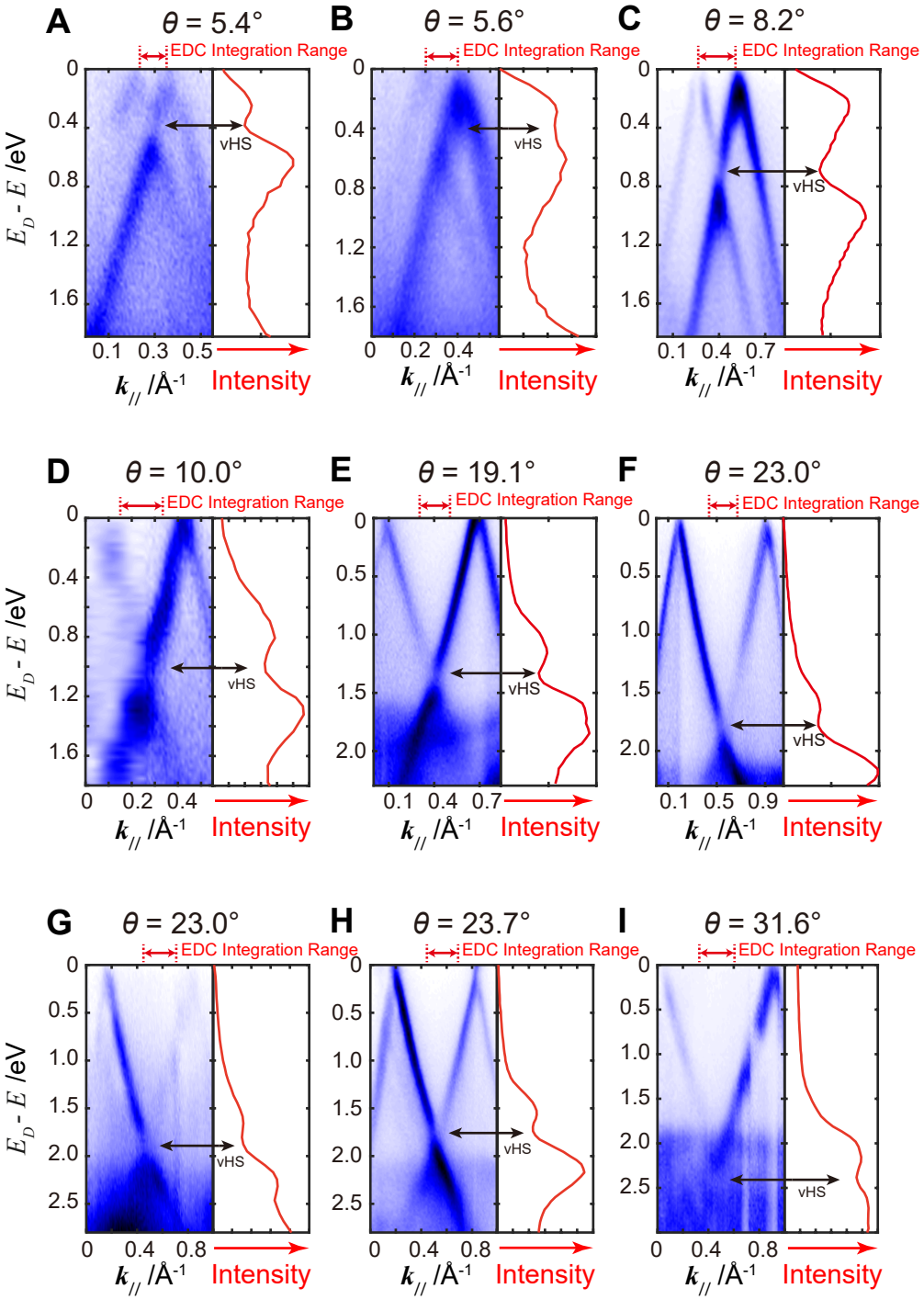

Figure 3.4: Band structure evolution with twist angle. Energy-momentum dispersion map from different twist angles. Thu cutting direction is through two K points and the vHS.

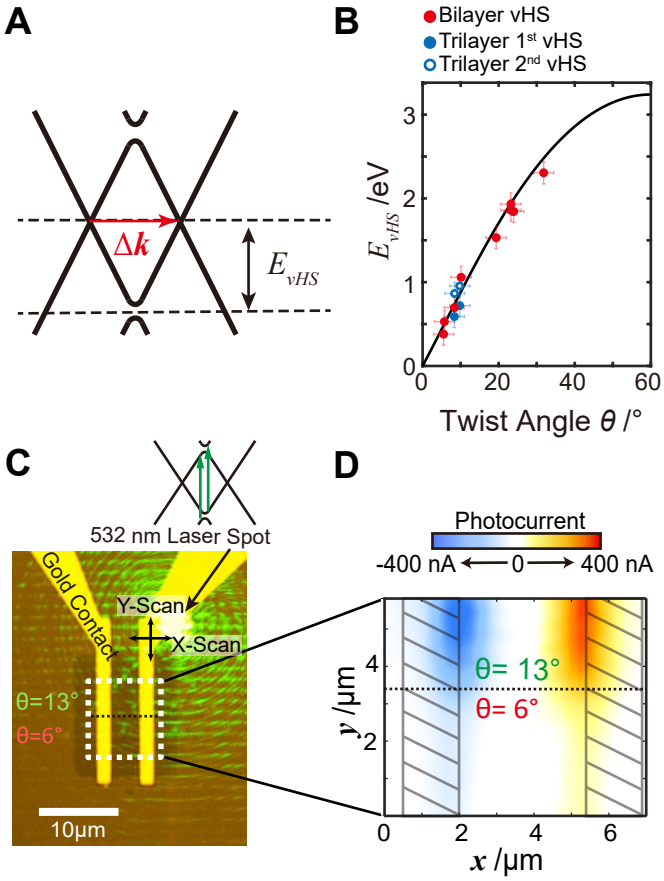

Figure 3.5: Summary of experiment data showing the twist angle dependence of vHS. A. Illustration of the relationship between $\Delta \boldsymbol{k}$ and the binding energy of vHS. As the twist angle θ increases, the separation between the two Dirac cones from each layer, $\Delta \boldsymbol{k}$, increases as well, which results in larger banding energy of the crossing point, i.e. vHS. **B.** Relationship between twist angle and the binding energy of vHS, E_{vHS}; the red and blue dots indicate the experimental results, while the black line is the predicted evolution by the theoretical model, showing the nonlinearity of the vHS binding energy at large twist angles. **C.** Optical image of a Photodetector with two regions of tBLG with varying twist angle under the illumination of a 532 nm laser. The insets show that the vHS pair will result in large response to the impeding laser with the photon energy that double the vHS binding energy. **D.** Real space mapping of the photocurrent during illumination. The two twist angle regions respond differently to the excitation wavelength. The 13° area corresponds to $2E_{vHS}$ of 2.3 eV, while the 6° area corresponds to $2E_{vHS}$ of 1.1 eV. The photon energy for the 532 nm laser is 2.3 eV.

rotation, a theoretical curve of vHS binding energy evolution with the twist angle can be produced, as shown by the black curve in 3.5.B. The deviation from a linear relationship between vHS binding energy and the twist angle stems from the non-linearity of the graphene electronic band structure at large binding energies. The experimental observation of the binding energy for the vHS is concluded in the same figure and agrees well with the theory. For comparison, the two observations of the twisted trilayer graphene (discussed in Section 3.4) is also included in Figure 3.5.B, showing two vHSs from each data. Thus, we systematically studied the twist bilayer graphene band strucutre in the angle range between 5° to 31° and find a neat dependency curve between the vHS binding energy and the twist angle.

3.3.2 Photocurrent enhancement with selective wavelength

Given the greatly enhanced carrier density of states at the vHS binding energy, it is possible to design a photodetector that is most sensitive to a certain wavelength ($E_{photon} = 2E_{vHS}$). Furthermore, the broad tunablity of the vHS binding energy (by changing the twist angle) demonstrated from our measurements (up to 2.5 eV, see Figure 3.5.B) guarantees the broad operation range from infrared to ultraviolet (up to 5 eV) photons.

A proof-of-concept device has been fabricated to demonstrate such application, as illustrated in Figures 3.5, C and D. We pattern two bilayer graphene domains with different twist angles of 13° and 6° (corresponding to the $2E_{vHS}$ of 2.3 eV and 1.1 eV, respectively). We then scan a focused laser beam (532 nm, $E_{photon} =$ 2.3 eV) with spot size of $\sim$ 1µm over the device, while the induced short-circuit photocurrent is recorded as a function of laser spot positions. Remarkably, in region 1 (13° twist angle) where the resonance absorption condition ($E_{photon} =$ $2E_{vHS} = 2.3$ eV) is met, the photocurrent is greatly enhanced (by 600%) compared to region 2 (6° twist angle), clearly demonstrating the feasibility and potential of the wavelength-selection application.

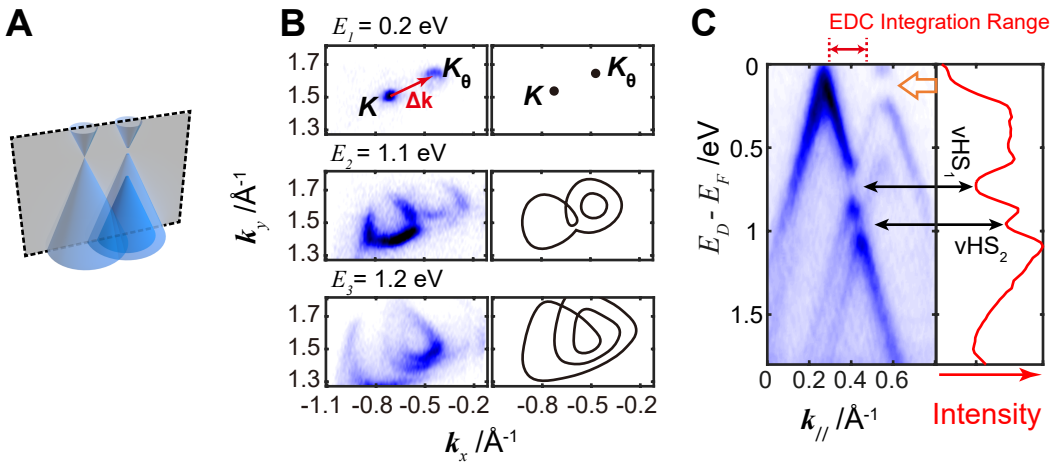

Figure 3.6: Van Hove Singularities in twisted trilayer graphene. A. Illustration of tTLG band structure. The left cone originates from the twisted top layer. The right double cone originates from the A-B-stacked middle and under layers. **B.** The left panel shows equal energy contours for the tTLG band structure data, with the illustration for the band structure in the right panel. **C.** Energy-momentum dispersion map of tTLG band structure, with cutting direction shown in Figure 3.2.D. The right panel shows integrated EDC over the region shown above. The tTLG dispersion presents two van Hove Singularities (marked with black arrows) with a difference in binding energy of $\sim 0.2\,\text{eV}$. There is also a gap opening (marked with the orange arrow) at $k_{||} \approx 0.6\,\text{Å}^{-1}$ with size $\Delta E_g^{ob} \sim 0.15\,\text{eV}$

3.4 Band structure of twisted trilayer graphene

As mentioned in the previous sections, twisted trilayer graphene (tTLG) is observed from spatial scanning image and further investigated by ARPES measurement. Typical tTLG observed in the experiment presents a Twist-A-B structure (Figure 3.6). As illustrated in Figure 3.6.A, the dispersions are composed of a single Dirac cone dispersion (on the left, originated from the top layer) and a double layer graphene dispersion with weaker intensity (on the right, originated from the bottom A-B stack). An apparent gap wit size $\Delta E_g^{ob} \sim 0.15\,\text{eV}$ between the conduction and valence band from the A-B stack is opened due to the existence of the electric potential difference between the two A-B-stacked layers [25][26], which is a result from the electric field from the capacitor as discussed in Section 2.3. In fact, using the fitting result of the effective capacitor model from Section 2.3, we can calculate the strength of the electric field among the AB-stacked layers and thus calculate the theoretical gap opening to compare with the experiment.

Recall Equation 2.9 for the three-layer system:

$$\begin{cases} \alpha\left(\Delta E_{F31}^2 + \Delta E_{F32}^2 + \Delta E_{F33}^2\right) - \Delta E_{F31} + W_{eff} = 0 \\ \alpha\Delta E_{F32}^2 - \Delta E_{F32} + \Delta E_{F31} = 0 \\ \alpha\Delta E_{F33}^2 - \Delta E_{F33} + \Delta E_{F32} = 0 \end{cases} \tag{3.1}$$

in which $\alpha^{fit} = 1.80\,\mathrm{eV}^{-1}$ and $W_{eff}^{fit} = -1.09\,\mathrm{eV}$. We can solve this equation system and have

$$\Delta E_{F31} = -0.46\,\mathrm{eV}$$

$$\Delta E_{F32} = -0.30\,\mathrm{eV}$$

$$\Delta E_{F33} = -0.21\,\mathrm{eV}$$

The electric potential energy difference between the AB-stacked layers (which are lower layers. Will be discussed in Section 3.5) is $eU = \Delta E_{F32} - \Delta E_{F31} = 0.16\ eV$.

Following the theory of A-B stacked graphene band structure in Reference [25, 26], the gap between the conduction band and valence band is predicted by

$$\Delta E_g = \sqrt{\frac{e^2U^2t^2}{e^2U^2 + t^2}}$$

where t ($\sim 0.22\,\mathrm{eV}$ [26]) is inter-layer hopping energy. With eU known from the capacitor model, the predicted band gap $\Delta E_g \sim 0.13\,\mathrm{eV}$, which is very near to the observed value ($\Delta E_g^{ob} \sim 0.15\,\mathrm{eV}$).

More interestingly, the ARPES measurement in Figure 3.6 shows that at the crossing points of the single layer and the bilayer dispersion, two vHSs are formed, as is observable both in the band dispersion plot and the spectral intensity plot. The two vHSs present a separation of $\sim 0.2\,\mathrm{eV}$, as is expected from the separation between two bands in A-B stacked graphene [3].

3.5 Layer arrangement for the twisted multilayer graphene

As discussed in Section 2.2, the graphene layers will absorb photoelectrons from the underlying substrate, which results in a contrast in the integrated spectrum intensity

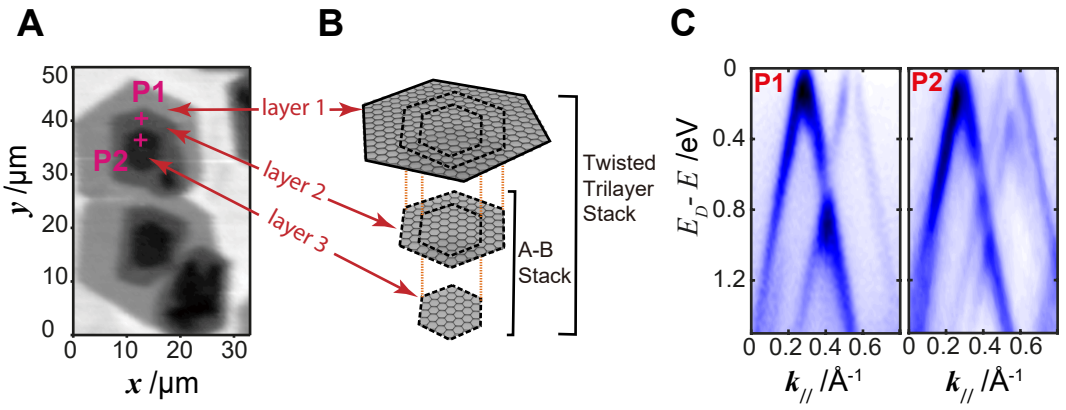

Figure 3.7: Layer arrangement for the twisted multilayer graphene. A. Spatial map of twisted Multilayer Graphene shown in Figure 3.1.D. As the colour darkens, the number of layer increases. Position 1 (marked as P1) is tBLG region and the adjacent Position 2 (marked as P2) is tTLG region. The band structure measured from P1 and P2 are presented in C. **B.** Lattice structure of tTLG. The bottom and the middle layers are Bernal stacked, while the top layer is rotated by a twist angle θ relative to underlying layers. **C.** Left panel: the energy-momentum dispersion map of the tBLG band structure measured in P1. Right panel: the energy-momentum dispersion map of the tTLG band structure measured in P2. The separations of the cones from different layers in the two maps are the same, indicating the single crystal nature of the top layer and the middle layer.

for regions with different layer number. We use this contrast to count the number of layers in Figure 3.7.A (also shown in Figure 3.1). We find both monolayer, bilayer and trilayer regions, with the multilayer domain surrounded by the fewer-layer region. An intuitive guess for the formation of this sample morphology is that the graphene layers stack one above another. But a less intuitive result is about the stacking order of the layers: We shall then show from further ARPES measurement: the largest graphene sheet (layer 1) is the topmost layer while the smaller ones go to the middle (layer 2) and the bottom (layer 3), as as illustrated in Figure 3.7.B.

Figure 3.7.C show the energy-momentum dispersion maps measured at the adjacent regions P1 and P2, respectively. The ARPES measurement on P1 presents tBLG band structure, with two Dirac cones intersecting and creates a vHS, and P2 presents tTLG band structure, with one Dirac cone intersecting with an A-B stacked bilayer double cone in the right, creating two vHSs. It is inferred from the intensity that the left Dirac cone comes from the top layer (with stronger

intensity) while the right double cone comes from the middle and bottom layers (with weaker intensity), indicating that the middle layer and the bottom layer are A-B stacked. Band structures from P1 and P2 show the same twist angle (8.2°) so that we can infer that they share the same twisted top layer and the middle layer. Now we can conclude that the top layer is larger than bottom layers, forming an inverted pyramid structure in Figure 3.7.B. This result agrees with the discussion in Reference [27], which shows the similar layer arrangement in the graphene layers grown by the similar CVD method.

3.6 Discussion and conclusion

Recent theoretical and transport studies reported a band gap opening at the Dirac points [28–32]. However, due to the limit of experimental resolution, the suggested band gap is not clearly observed in the present study.

Our experimental results clearly establish that interlayer coupling between graphene layers is present over a broad twist angle (up to 31°), thus greatly extending the range ($1° - 10°$) of inter-layer coupling suggested by previous STM/STS studies [18]. We also note that the large angle coupling reported here stands in contrast to some STM/STS studies [20, 21] that report the disappearance of vHSs above a twist angle of 5.5° and 20°, respectively. The difference in the findings may result from different sample quality and/or the differences in the measurement positions.

On the other hand, recent optical studies also reported enhanced absorption and optical conductivity at energies that could correspond to the VHS binding energy at large twist angles [16, 17, 22]. However, there is a competing interpretation for these optical results, which is based on optical enhancement by parallel bands of two twisted Dirac cones [22] and does not require the existence of vHS. Thus our study constitutes the first direct evidence for the existence of the vHS in twisted bi- and multilayer graphene at large twist angles. In addition to the interlayer coupling at large twist angle, we also demonstrated that bi- and multilayer graphene could be used in wavelength selective photodetection, thus opening up the door for

applying twisted bi-and multilayer graphene in optoelectronic applications ranging from the infrared to the ultraviolet regime.

As our experiment systematically established the twist angle evolution of the electronic structure and van Hove singularity in twisted bilayer graphene in the angle regime 5.4° to 31.6°, it is worth looking at the smaller angles in future studies. By the time this thesis was completed, we learned of the very recent discovery of the strong modulation of the electronic structure in the twist bilayer graphene with 'magical angles' ($\sim 1.1°$), resulting in correlated insulator behaviour [33] and unconventional superconductivity [34]. A future ARPES study in twisted few-layer graphene with nearby twist angles will provide further physical insight for tuning the electronic structures in these exotic quantum phases.

Experimental section

Twisted few-layer graphene (tFLG) samples are grown on copper foil via chemical vapour deposition (CVD) [35] by our collaborators from Peking University (Dr Huan Wang, Dr Jianbo Yin, Prof Hailin Peng). Micro-ARPES experiments are performed at the Spectromicroscopy beamline at the Elettra synchrotron in Trieste, Italy [36] and ANTARES beamline at the SOLEIL synchrotron in Paris, France [37]. The measurements are done under a base pressure of 10^{-10}mbar in ultra-high vacuum and the sample kept at the temperature 110 K to minimize the thermal broadening of the spectra. The spectra are taken at a photon energy of 74 eV in Elettra, 100 eV in Soleil, with estimated energy and angular resolution of ~ 50 meV and $\sim 0.5°$, respectively. Before transferring into the photoemission acquisition chamber, the samples are annealed at 350 °C for 30 min in a preparation chamber with base pressure 10^{-10}mbar to remove H_2O and other contaminants adsorbed during the transfer in air.

Bibliography

[1] KSA Novoselov et al. “Two-dimensional gas of massless Dirac fermions in graphene”. In: *Nature* 438.7065 (2005), pp. 197–200.

[2] Yuanbo Zhang et al. “Experimental observation of the quantum Hall effect and Berry’s phase in graphene”. In: *Nature* 438.7065 (2005), pp. 201–204.

[3] A. H. Castro Neto et al. “The electronic properties of graphene”. In: *Reviews of Modern Physics* 81.1 (2009), pp. 109–162.

[4] Xinran Wang et al. “N-doping of graphene through electrothermal reactions with ammonia”. In: *Science* 324.5928 (2009), pp. 768–771.

[5] Phaedon Avouris. “Graphene: electronic and photonic properties and devices”. In: *Nano Letters* 10.11 (2010), pp. 4285–4294.

[6] Lei Liao et al. “High-speed graphene transistors with a self-aligned nanowire gate”. In: *Nature* 467.7313 (2010), pp. 305–308.

[7] Frank Schwierz. “Graphene transistors”. In: *Nature Nanotechnology* 5.7 (2010), pp. 487–496.

[8] F. Bonaccorso et al. “Graphene photonics and optoelectronics”. In: *Nature Photonics* 4.9 (2010), pp. 611–622.

[9] Ming Liu et al. “A graphene-based broadband optical modulator”. In: *Nature* 474.7349 (2011), pp. 64–67.

[10] F. Xia et al. “Ultrafast graphene photodetector”. In: *Nature Nanotechnology* 4.12 (2009), pp. 839–43. URL: `http://www.ncbi.nlm.nih.gov/pubmed/19893532`.

[11] J. M. B. Lopes dos Santos, N. M. R. Peres, and A. H. Castro Neto. “Graphene Bilayer with a Twist: Electronic Structure”. In: *Physical Review Letters* 99.25 (2007).

[12] Guohong Li et al. “Observation of Van Hove singularities in twisted graphene layers”. In: *Nature Physics* 6.2 (2009), pp. 109–113.

[13] W. Landgraf et al. “Electronic structure of twisted graphene flakes”. In: *Physical Review B* 87.7 (2013).

[14] S. Shallcross, S. Sharma, and O. Pankratov. “Emergent momentum scale, localization, and van Hove singularities in the graphene twist bilayer”. In: *Physical Review B* 87.24 (2013).

[15] Taisuke Ohta et al. “Evidence for Interlayer Coupling and Moiré Periodic Potentials in Twisted Bilayer Graphene”. In: *Physical Review Letters* 109.18 (2012).

[16] Pilkyung Moon and Mikito Koshino. “Optical absorption in twisted bilayer graphene”. In: *Physical Review B* 87.20 (2013).

[17] R. W. Havener et al. “Van Hove singularities and excitonic effects in the optical conductivity of twisted bilayer graphene”. In: *Nano Letters* 14.6 (2014), pp. 3353–7. URL: http://www.ncbi.nlm.nih.gov/pubmed/24798502.

[18] I. Brihuega et al. “Unraveling the intrinsic and robust nature of van Hove singularities in twisted bilayer graphene by scanning tunneling microscopy and theoretical analysis”. In: *Physical Review Letters* 109.19 (2012), p. 196802. URL: http://www.ncbi.nlm.nih.gov/pubmed/23215414.

[19] Kazuyuki Uchida et al. “Atomic corrugation and electron localization due to Moiré patterns in twisted bilayer graphenes”. In: *Physical Review B* 90.15 (2014).

[20] Wei Yan et al. “Angle-dependent van Hove singularities and their breakdown in twisted graphene bilayers”. In: *Physical Review B* 90.11 (2014).

[21] A. Luican et al. “Single-Layer Behavior and Its Breakdown in Twisted Graphene Layers”. In: *Physical Review Letters* 106.12 (2011).

[22] R. W. Havener et al. “Angle-resolved Raman imaging of interlayer rotations and interactions in twisted bilayer graphene”. In: *Nano Letters* 12.6 (2012), pp. 3162–7. URL: http://www.ncbi.nlm.nih.gov/pubmed/22612855.

[23] K. Kim et al. “Raman spectroscopy study of rotated double-layer graphene: misorientation-angle dependence of electronic structure”. In: *Physical Review Letters* 108.24 (2012), p. 246103. URL: http://www.ncbi.nlm.nih.gov/pubmed/23004295.

[24] R. He et al. “Observation of low energy Raman modes in twisted bilayer graphene”. In: *Nano Letters* 13.8 (2013), pp. 3594–601. URL: http://www.ncbi.nlm.nih.gov/pubmed/23859121.

[25] Taisuke Ohta et al. “Controlling the electronic structure of bilayer graphene”. In: *Science* 313.5789 (2006), pp. 951–954.

[26] Eduardo V Castro et al. “Biased bilayer graphene: semiconductor with a gap tunable by the electric field effect”. In: *Physical Review Letters* 99.21 (2007), p. 216802.

[27] Shu Nie et al. “Growth from below: bilayer graphene on copper by chemical vapor deposition”. In: *New Journal of Physics* 14.9 (2012), p. 093028.

[28] E. J. Mele. “Commensuration and interlayer coherence in twisted bilayer graphene”. In: *Physical Review B* 81.16 (2010), p. 161405. URL: http://link.aps.org/doi/10.1103/PhysRevB.81.161405.

[29] Zhenhua Ni et al. “*G*-band Raman double resonance in twisted bilayer graphene: Evidence of band splitting and folding”. In: *Physical Review B* 80.12 (2009), p. 125404. URL: http://link.aps.org/doi/10.1103/PhysRevB.80.125404.

[30] Jeongho Park et al. “Observation of the intrinsic bandgap behaviour in as-grown epitaxial twisted graphene”. In: *Nature Communications* 6 (2015).

[31] A. V. Rozhkov et al. “Single-electron gap in the spectrum of twisted bilayer graphene”. In: *Physical Review B* 95.4 (2017), p. 045119. URL: http://link.aps.org/doi/10.1103/PhysRevB.95.045119.

[32] A. O. Sboychakov et al. “Electronic spectrum of twisted bilayer graphene”. In: *Physical Review B* 92.7 (2015), p. 075402. URL: http://link.aps.org/doi/10.1103/PhysRevB.92.075402.

[33] Yuan Cao et al. “Correlated insulator behaviour at half-filling in magic-angle graphene superlattices”. In: *Nature* 556.7699 (2018), p. 80.

[34] Yuan Cao et al. “Unconventional superconductivity in magic-angle graphene superlattices”. In: *Nature* 556.7699 (2018), p. 43.

[35] Cecilia Mattevi, Hokwon Kim, and Manish Chhowalla. “A review of chemical vapour deposition of graphene on copper”. In: *Journal of Materials Chemistry* 21.10 (2011), pp. 3324–3334.

[36] Pavel Dudin et al. “Angle-resolved photoemission spectroscopy and imaging with a submicrometre probe at the SPECTROMICROSCOPY-3.2 L beamline of Elettra”. In: *Journal of Synchrotron Radiation* 17.4 (2010), pp. 445–450.

[37] Jose Avila et al. “ANTARES, a scanning photoemission microscopy beamline at SOLEIL”. In: *Journal of Physics: Conference Series* 425.19 (2013), p. 192023.

4

Extracting energy band from ARPES data: a neural network approach

Contents

Finding peaks in two dimensional (2D) data is a common practice in ARPES data analysis, which is typically achieved by computing the local derivatives. However, this method is inherently unstable when the local landscape is complicated, or the signal-to-noise ratio of the data is low. In this chapter, we propose a new method in which the peak tracking task is formalized as an image inverse problem, and thus can be solved with a convolutional neural network (CNN). In addition, we show

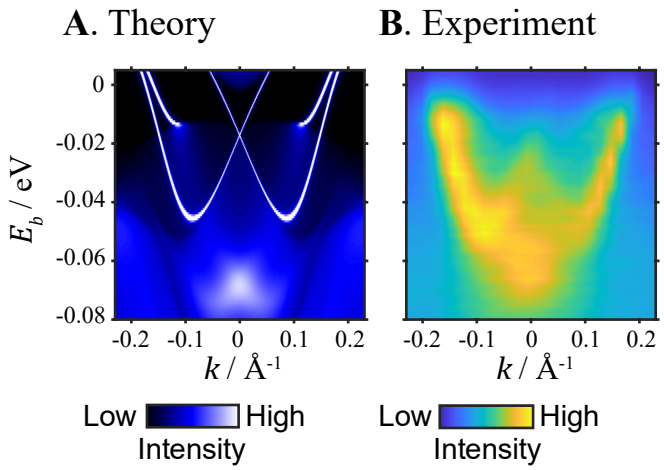

Figure 4.1: Example of theoretical energy band and ARPES data. A. Density functional theory calculation of the band structure of $NbIrTe_4$. The brighter color shows higher intensity. **B.** The corresponding experiment data of the band structure. The energy band is blurred and noisy.

that the underlying physics principle of the experiments can be used to generate the training data. By generalizing the trained neural network on real experimental data, we show that the CNN method can achieve comparable or better results than traditional derivative based approach. Our results could be further generalized in different physics experiments when the physical process is known.

4.1 Introduction

4.1.1 Introduction to ARPES energy band extraction

Recent advances on experimental techniques in condensed matter physics boost the generation of large volume high-quality data in modern physics experiments. In order to present these data, 2D (and even 3D) representations of the data becomes more and more popular, such as in angule-resolved photoemission spectroscopy (ARPES) [1], scanning tunneling microscopy (STM) [2], resonant inelastic x-ray scattering (RIXS) [3], etc. In these experiments, as the data quality is often limited by the instrumental resolution and different intrinsic physical processes, the retrieving of physical quantities with high precision from these volume data can therefore benefit from effective analysis methods.

As an example, a typical 2D ARPES experiment data set is shown in Figure 4.1. Ideally, the ARPES spectra will follow the theoretical energy-momentum dispersion shown in Figure 4.1.A. However, intrinsic broadening effects [1] such as electronic correlation, as well as extrinsic factors such as crystal defects can broadens the spectrum in both energy and momentum dimensions. Together with the resolution limitation, sometimes it is difficult to resolve the energy bands in the 2D measurements (e.g. in Figure 4.1.B). To enhance the features in the 2D band dispersions, several derivative based methods have been proposed, such as the Maximum Curvature method [4] and the Minimum Gradient method [5]. The Maximum Curvature method [4] calculates the local curvature and assumes the pixels with the largest curvature are the positions of the energy bands; the Minimum Gradient method [5] calculates the average gradient and assumes the positions with the lowest average gradient represent the energy band location. However, these methods can only achieve best results in high signal-to-noise ratio data and tend to fail in complicated situations when multiple bands are close to each other or when the data are too noisy.

On the other hand, recent development of convolutional neural network (CNN) provides great performance in improving 2D data quality, such as super-resolution, denoising and patching [6–8]. As high-resolution reference 2D data are subjected to various degrading transformations, the objective of our data analysis becomes finding an appropriate inverse transformation that can best recover the original reference 2D images – which can be formulated as solving an inverse problem.

Motivated by this understanding, we consider the energy band extraction problem in a 2D ARPES image (broadened by the intrinsic and extrinsic processes as discussed above) as a problem of inversing the physical processes that blurs the spectral peaks along the band dispersions, and thus it can be treated using CNN. In other words, we effectively look for a map between the "broadened experimental dispersions" and the "original dispersions". Moreover, leveraging the existing knowledge of the intrinsic and extrinsic broadening processes, massive simulated

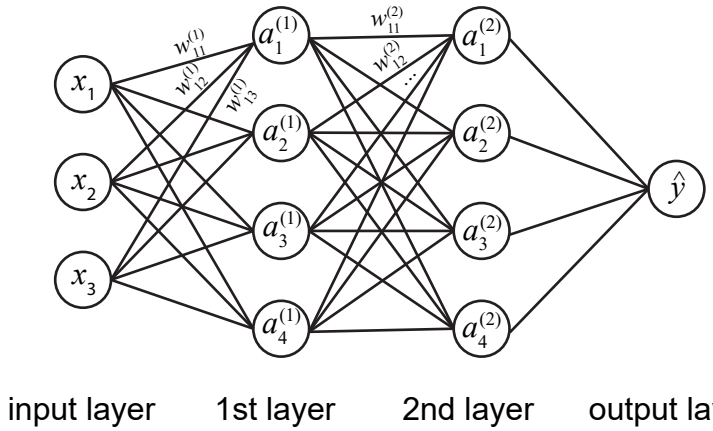

Figure 4.2: A typical neural network. The nodes are the neurons. The edges show the connection among the neurons.

data can be generated for the training purpose before we apply the trained model to the real experimental data.

4.1.2 Introduction to neural network

Before diving into the details of CNN in ARPES data processing, we first briefly review the concept of the neural network. A pedagogical chapter of the neural network can be found in Chapter 5 of Reference [9]. A timely review can be found in Reference [10] for the neural network and its applications.

Neural networks were firstly proposed to simulate the information processing of neurons [11] and then widely used in machine learning [10] for different tasks such as speech recognition, image classification and object detection.

As shown in Figure 4.2, a typical neural network consists of activation units (neurons) arranged in a layered fashion [9]. The exemplary neural network can be used to classify the points in the 3D space. The input is the coordinates of a point in a 3D space (x_1, x_2, x_3). The output $\hat{y}$ is a prediction about how likely the point belongs to a certain area (when the output $\hat{y}$ is near 1) or does not belong to that area (when $\hat{y}$ is near 0). The 'edges' between the neurons show the chain of the functional relationship: The input (x_i) of the network is passed to the neurons in the first hidden layer to calculate the intermediate variables $(a_i^{(1)})$, which are then

passed to the neurons in the second hidden layer ($a_i^{(2)}$). Finally, the variables in the second layer are passed to the output layer to produce the final result ($\hat{y}$).

The connections between the neurons take the form of a linear combination of the early layer following an 'activation function' $f(z)$, i.e.:

$$a_i^{(l)} = f(\sum_j w_{ij}^{(l)} a_j^{(l-1)} + b^{(l)}), l = 1, 2$$

$$\hat{y} = \text{Sigmoid}(\sum_j w_{ij}^{(3)} a_j^{(2)} + b^{(3)})$$

The activation function $f(z)$ is typically a sigmoid function ($f(z) = 1/(1+\exp(-z))$), a tanh function, or a rectified linear unit ($f(z) = \max(z, 0)$) [12]. The parameters $w_{ij}^{(l)}$ are called weights and $b^{(l)}$ are bias. In the first layer, the input $a_j^0 = x_j$.

A loss function is defined to describe the performance of the neural network. For a classification problem, the loss function is typically defined as

$$\mathscr{L}(y, \hat{y}) = -(y\log(\hat{y}) + (1-y)\log(1-\hat{y})$$

y is the correct classification (1 or 0) of the data point, or 'label'. When the label $y = 1$ and the output $\hat{y}$ is near 1, $\mathscr{L}$ will be close to 0. When $y = 1$ and $\hat{y}$ is near 0, $\mathscr{L}$ will be very large. The smaller $\mathscr{L}$ is, the better the neural network performs.

Instead of setting the parameters by hand, the neural network is trained. The method called 'back propagation' is widely used for the training [13][10]. The core idea is to calculate the derivatives (gradients) of the loss function against the parameters. The calculation of the gradients follows the chain rule of partial derivative. By shifting the parameters towards the opposite direction of the gradients in the prameter space, the loss function can be minimized. There are a few variations of the back propagation, such as the Adam [14] which adjusts the step size for each iteration.

In a typical fully-connected neural network architecture, the l-th-layer neuron $a_i^{(l)}$ collects information from all the neurons in the previous layer. This can result in a large number of weights and cause difficulties in computing. With some additional assumption, the standard neural networks can be modified to reduce the number of parameters without losing performance. Convolutional neural network is a variation

of neural network which is widely used for imaging data [10]. The underlying assumption is that the image can be decomposed as basic features such as edges and patches, which are shift-invariant. The existence of these features can be detected by convolving the image with the filters corresponding to different features, creating a responding feature map. The feature map is then used as the input of the next layer. Note that convolution is also a linear combination of the pixel values from an image, and the filters are the weights. Thus, the filters can be learned through training with back propagation, forming an efficient representation of images [10].

In this chapter, we use the simulated ARPES data to train a Super-Resolution Convolutional Neural Network (SR-CNN) that fits the ARPES experiments' spectral intensity map with the extrema feature map, and thus highlights the positions of the energy bands. SR-CNN was originally proposed for mapping low resolution image patches to corresponding high resolution patches, which is an inverse problem of down sampling in image processing [6]. Comparing to other recent neural network architectures in solving this problem that uses a very deep net [7, 8], the SR-CNN has only three layers and the function of each layer can be well understood. We demonstrate that this method can resolve complicated features in ARPES data and outperforms previous traditional algorithms in noise-resilience, sharpness and accuracy.

4.2 Architecture of super-resolution convolutional neural network

4.2.1 Design of the convolutional neural network architecture

The design of our convolutional neural network was modified from the super-resolution convolutional neural network (SR-CNN), a three-layer fully convolutional neural network proposed by Dong, Loy, He and Tang for image super-resolution [15].

The architecture of our modified neural network is shown in Figure 4.3 In SR-CNN, each layer is understood as an operation that is comparable to the traditional image restoration methods [6, 15]. The first layer transforms the raw experimental

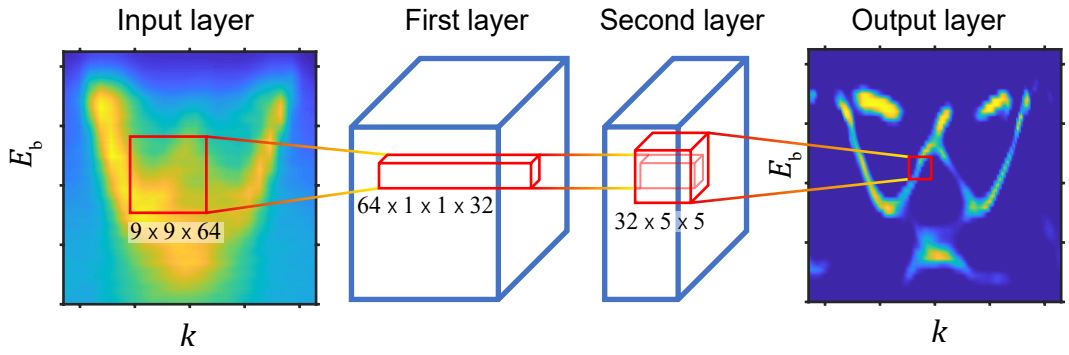

Figure 4.3: Architecture of the convolutional neural network for ARPES band extraction. The forward propagation from the experiment data (blurry) to the energy band feature map (sharp). The input layer: an experimental energy-momentum intensity distribution map. The first layer: convolution of the input layer with 64 filters with the size 9-by-9-by-1 with the ReLU activation function. The second layer: convolution with 32 filters with size 1-by-1-by-64 filters with the ReLU activation function. Output layer: convolution with a 5-by-5-by-32 filter with the Sigmoid activation function.

image patches to an n_1-dimensional representation under a trained basis set. The second layer non-linearly maps the new representation to the n_2-dimensional sharp energy band feature space. At the final stage, the image of the energy band is reconstructed by averaging all the features from the adjacent area. Assuming $\mathbf{Y}$ is the input image (note that we use the notation $\mathbf{Y}$ instead of $\mathbf{X}$ as the input to show that it is an inverse problem), W_i and B_i are the weights and bias in the i-th layer, this three-layer neural network can be mathematically written as:

$$F_1(\mathbf{Y}) = \max(0, W_1 * \mathbf{Y} + B_1)$$

$$F_2(\mathbf{Y}) = \max(0, W_2 * F_1(\mathbf{Y}) + B_2)$$

$$F(\mathbf{Y}) = \text{sigmoid}(W_3 * F_2(\mathbf{Y}) + B_3)$$

The $*$ denotes a convolution. The result of the convolution in the first two layers is passed to a rectified linear unit (ReLU, $\max(0, x)$) to produce non-linearity [16]. The output layer is with a sigmoid activation function ($\text{sigmoid}(x) = 1/(1 + e^{-x})$).

Note that although the architecture we are using is almost the same as SR-CNN, the problem we are trying to solve is different from what SR-CNN was originally designed for: In the original SR-CNN, the super-resolution problem was formulated as a regression problem, where no non-linear function was applied in the last

layer, and the mean squared error (MSE) loss between the network output and the label was minimized. In our design, the problem was formulated as h_{out}-by-w_{out} classification problem. The sigmoid activation function is applied in the third layer to obtain the confidence for the existence of the energy band. We minimize the standard loss function for classification, i.e. the cross entropy, also known as the negative log likelihood of the label, which is defined as

$$\mathscr{L}(\mathbf{X}, \hat{\mathbf{X}}) = -\frac{1}{N}\sum_{n=1}^{N}\{X_n \log(\hat{X}_n) + (1 - X_n)\log(1 - \hat{X}_n)\}$$

where X_n ($\hat{X}_n$) denotes for each pixel in the label (CNN output from the training data).

4.2.2 Dimensional analysis

The size of the inputs and outputs for each layer is examined closely for the implementation of the project.

In the **first layer**, we have $n_1 = 64$ filters with the width $f_1 = 9$. So, size(W_1) = $[n_1, f_1, f_1, 1]$. The padding for the numerical convolution is 'valid', which means the pixels near the input image boundary are discarded to ensure all outputs are proper result of the product-sum between the image patch and the filter, instead of involving 0-padding. Assuming the input image size is h_{in}-by-w_{in}, the output $F_1(\mathbf{Y})$ should have the size of $(h_{in} - f_1 + 1)$-by-$w_{in} - f_1 + 1$ ($(h_{in} - 8)$-by-$w_{in} - 8$ in our setting).

For the **second layer**, we have $n_2 = 32$ filters with the width $f_2 = 1$. So, size(W_2) = $[n_2, 1, 1, n_1]$. The output $F_2(\mathbf{Y})$ should have the size of $(h_{in} - f_1 + 1 - f_2 + 1)$-by-$w_{in} - f_1 + 1 - f_2 + 1$ ($(h_{in} - 8)$-by-$w_{in} - 8$ in this setting).

For the **third layer**, we have 1 filter of the width $f_3 = 5$. So, size(W_3) = $[1, f_3, f_3, n_2]$ and the final output size $(h_{in} - f_1 + 1 - f_2 + 1 - f_3 + 1)$ -by-$w_{in} - f_1 + 1 - f_2 + 1 - f_3 + 1$, which is $h_{out} = h_{in} - 12$, $w_{out} = w_{in} - 12$ in this case. Tracking down the convlution operations, we can immediately know that each output pixel is determined locally by the neighboring $13 - by - 13$ pixels in the input image, i.e. the receptive field of each output pixel is 13-by-13. This local-determination means the global property of an energy band will not affect the judgment of the CNN. Only the local features will be used to determine whether there is energy band or not.

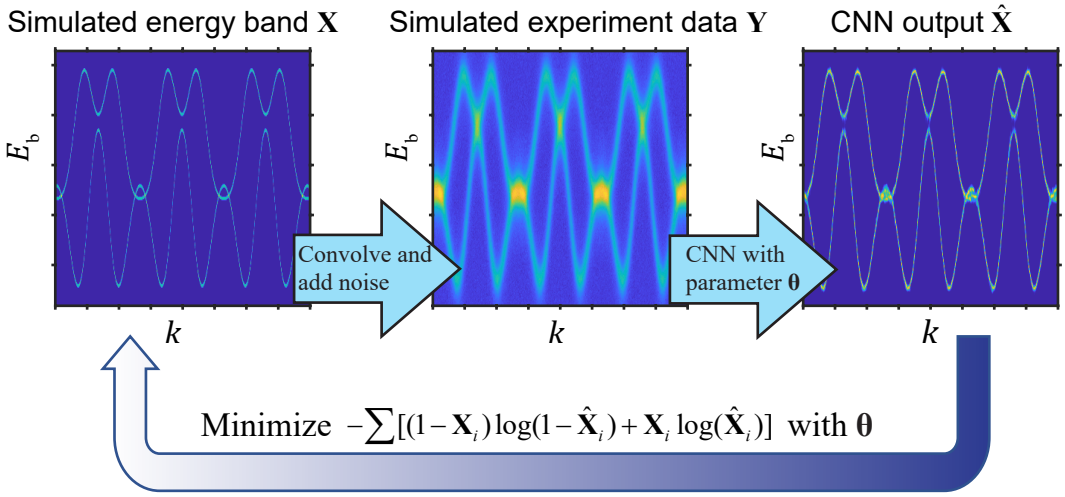

Figure 4.4: The training process using simulated data. Step 1. The training label $\mathbf{X}$ is generated by a random-parameterized tight binding model. **Step 2.** The training data $\mathbf{Y}$ is produced by Lorentzian and Gaussian convolution of the label and with random noise added. **Step 3.** The training data is used as the input for the convolutional neural network (CNN) to compute the output $\hat{\mathbf{X}}$. **Step 4.** CNN output $\hat{\mathbf{X}}$ is then compared with the label $\mathbf{X}$ to calculate the gradient. The resulted gradient is used to minimize the loss function iteratively.

4.3 Training the neural network

4.3.1 Generation of simulated data for training

For a low-level vision task such as super-resolution, the training process follows the paradigm of unsupervised learning. The inputs of the model are generated by down-sampling the high-resolution image patches in the training set. The output generated from the forward propagation process is then compared with the original high-resolution image to compute the loss function. Backpropagation is used to minimize the loss function $\mathscr{L}$ iteratively. In this process, the high-resolution image patches are used as label, and the down-sampled ones are used as input of the model [6].

For the task of the energy band feature extraction from the experiment data, the training data and the label should be chosen more carefully. For any experiment data, it is not possible to label the energy band position automatically and it is not accurate to label it by hand. To solve this dilemma, simulated data is used for the training and testing process while the experiment data is used to evaluate the model.

Figure 4.4 shows the data simulation and the training process. The energy

band $\epsilon(k)$ is generated through a tight binding model with randomized parameters. Since the SRCNN output is only affected locally by the neighboring 13-by-13 pixels, the global property such as symmetry of the energy band is not important. The energy band image is then generated by discretizing $\epsilon(k)$ through putting 1's in the occupied pixels and 0's in the unoccupied pixels. The generated image is finalized by super-sampling for anti-aliasing [17] and used as the label.

The key part is the generation of the simulated data with the label. The ARPES spectrum broadening model is well studied. Assuming we have an energy band with a shift due to self-energy: $E = \epsilon(\mathbf{k}) + \Sigma'(\mathbf{k}, E)$, the one-particle spectral function is written as

$$A(\mathbf{k}, E) = -\frac{1}{\pi} \frac{\Sigma''(\mathbf{k}, E)}{(E - \epsilon(\mathbf{k}) - \Sigma'(\mathbf{k}, E))^2 + \Sigma''(\mathbf{k}, E)^2}$$

which means the energy band is broadened by the self-energy that comes from the electronic interactions. And the observed data, the spectral intensity, follows

$$I_0(\mathbf{k}, E) \sim \{A(\mathbf{k}, E) FD(E) |M(\mathbf{k})|^2 + g_n^{in}(\mathbf{k}, E)\} * R(\Delta k, \Delta E) + g_n^{ex}(\mathbf{k}, E)$$

where $FD(E)$ is Fermi-Dirac distribution, $M(k)$ is the matrix element, $g_n^{in}(k, E)$ is the intrinsic noise such as the shot noise, $*$ denotes convolution, $R(\Delta k, \Delta E)$ is the instrument resolution and $g_n^{ex}(\mathbf{k}, E)$ is the extrinsic noise such as circuit noise.

In the expression of the spectral intensity, all the slow-variate part can be ignored in our model due to the localized, all-convolution network design. To generate the simulated data, the delta-function-like energy band image is convolved with the one-particle spectral of randomized self-energy and is added with a Poisson noise. Gaussian blurring is then applied to simulate the finite instrumental resolution. A Gaussian noise is added at the final step for the circuit noise. The finalized broadened and noisy simulated image is used as the training data.

The initial weights of the filters and bias are from the result of the SR-CNN trained with a natural image set [6]. The training data is passed through the forward propagation to produce the output. The loss function $\mathscr{L}$ is then calculated between the outputs and the labels to produce a gradient flow which determines the changing direction of parameters. An Adam optimizer is used for the backpropagation [14].

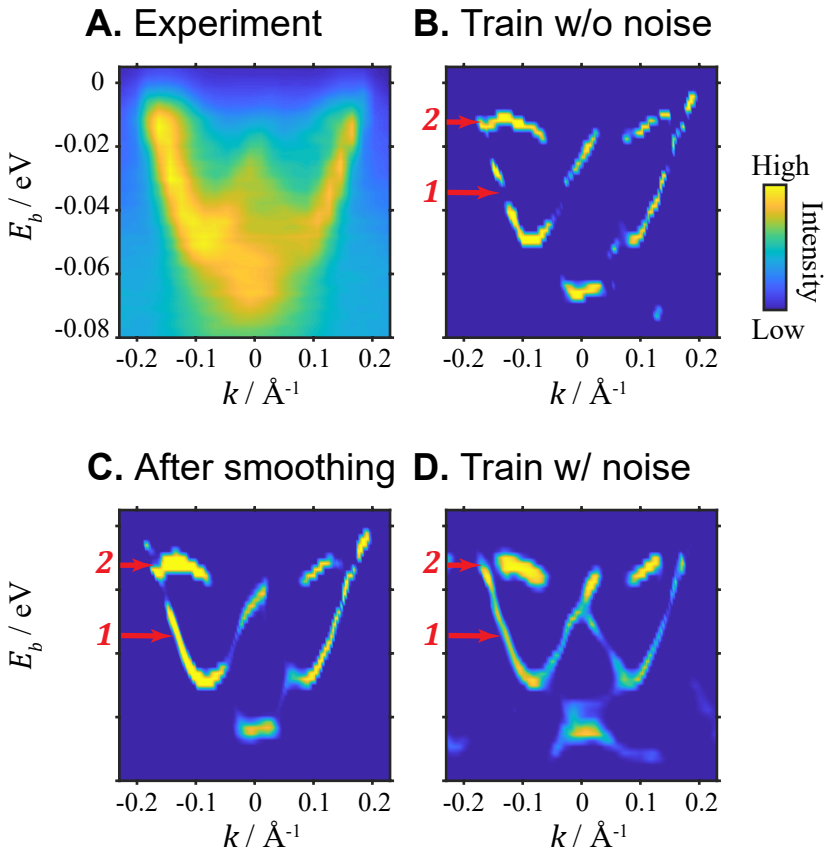

Figure 4.5: Training with noise to avoid overfitting. A. Experiment data in Figure 4.7, which is used to produce the subsequent results. **B.** The energy band extraction result using CNN, which is trained for 30M steps with noise-free simulated data. No pre-processing is used except for interpolation. The extracted band is discontinuous (marked with the red arrow 1). Two bands with small separation are not able to resolve (marked with the red arrow 2). **C.** The band extraction result using the same training method with B. but the experiment data is pre-processed with smoothing. The band is more continuous at the position marked by the red arrow 1 but the small feature is still not able to be resolved (marked by the red arrow 2) **D.** The band extraction result of CNN that is trained for 30M steps with noise-corrupted simulated data. No pre-processing is used except for interpolation. The band is continuous (marked with red arrow 1). The two near bands are clearly separated (marked with red arrow 2).

4.3.2 Prevention of over-fitting

One issue of neural network is over-fitting [9], when the training set is too small and the model fails to generalize to the other data sets. This issue should be tackled carefully when using simulated data, as shown in Figure 4.5. Since the experiment data is always noisy, a model trained with the noise-free simulated data may treat the experimental noise as separated peaks, resulting in discontinuity of the output

	Gap size	Gap size error	Peak width	Contrast
Original Data	30meV	-	77meV	-
CNN	24meV	18%	6meV	0.99
Maximum Curvature	25meV	15%	23meV	0.12
Minimum Gradient	N/A	N/A	16meV	N/A

Table 4.1: Performance benchmarking of different methods applied to the simulated data

energy band, as shown in Figure 4.5.B (marked with the red arrow 1). Smoothing is a common method to suppress the noise in both Maximum Curvature (MC) and Minimum Gradient (MG) methods and can also be applied to pre-processing in CNN. However, although the pre-smoothing step results in a continuous energy band image in 4.5.C, some of the small features are lost (marked with the red arrow 2). This problem is common in the MC and MG. To enhance the model's performance under noise and to avoid information loss from the smoothing step, random artificial noise is added in the training data. As a result, the output of the model for the experiment data shows a continuous energy band without any smoothing and keeps the detailed features (4.5.D).

4.4 Benchmark of the algorithm performance

To further compare the performance and the reliability of different data analysis methods, we apply each method to a variety of data sets, with the result presented in Figure 4.6 and Table 4.1 for the simulated data; in Figures 4.7 and 4.8 for the experiment data.

4.4.1 Quantitative benchmark with simulated data

Figure 4.6 compares the sensitivity to band gap for different methods. We applied each method to the simulated data with a small energy gap of $\sim 30\,\mathrm{meV}$. The gap is indistinguishable either from the visual inspection of the image or from the energy distribution curve. The results of different methods are summarized in Table 4.1. The Maximum Curvature method resolves the gap feature successfully,

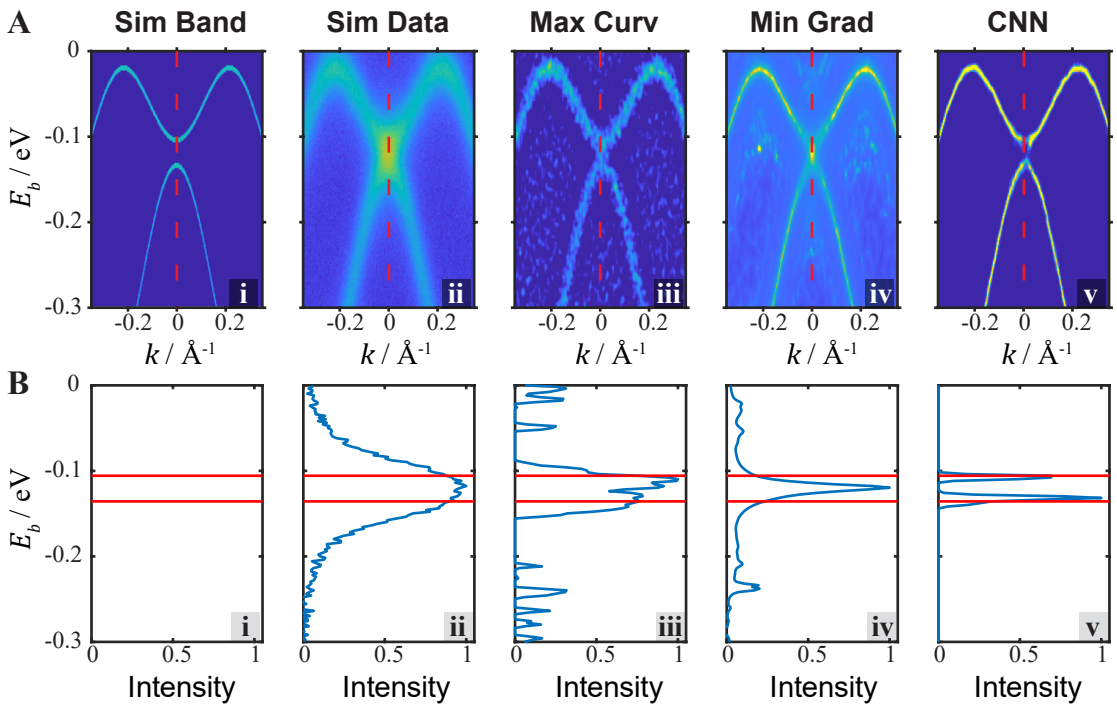

Figure 4.6: Performance analysis of different algorithms with simulated data. **A.** Performance of different methods on a simulated data. **i.** The simulated energy band map that is used to generate the data. A 30 meV gap is at the binding energy $E_b \sim -0.12$ eV **ii.** The noise-corrupted simulated data used in the following analysis. The small gap is not conceivable directly from the data. **iii.** – **v.** The energy band extraction result based on the simulated data, using the Maximum Curvature method (iii), Minimum Gradient method(iv) and the Convolutional Neural Network method (CNN) (v), respectively. **B.** The energy distribution curve of k = 0 from the corresponding map in A. (marked with the red dashed line in A.). The two red lines ($E_b = -0.394$ eV and -0.364 eV, respectively) mark the 30meV gap from the original energy band.

with an inferred gap size of 25 meV from fitting (Figures 4.6, A.iii and B.iii). The Minimum Gradient resolves most of the band clearly but falsely produces high intensity values inside the gap (Figures 4.6, A.iv and B.iv). This is because the local intensity landscape is a saddle point (minima long E direction but maxima along k direction), where the average gradient reaches minimum as it does in a peak point or a ridge. This saddle-point problem prevents Minimum Gradient method from resolving small gap feature in general. As shown in 4.6, A.v and B.v, CNN resolves the gap with the size 24 meV. Though MC and CNN provide the comparable results in gap size, the contrast of the CNN result is much larger and the resolved bands are sharper. Also, the result is more noise resilient in CNN.

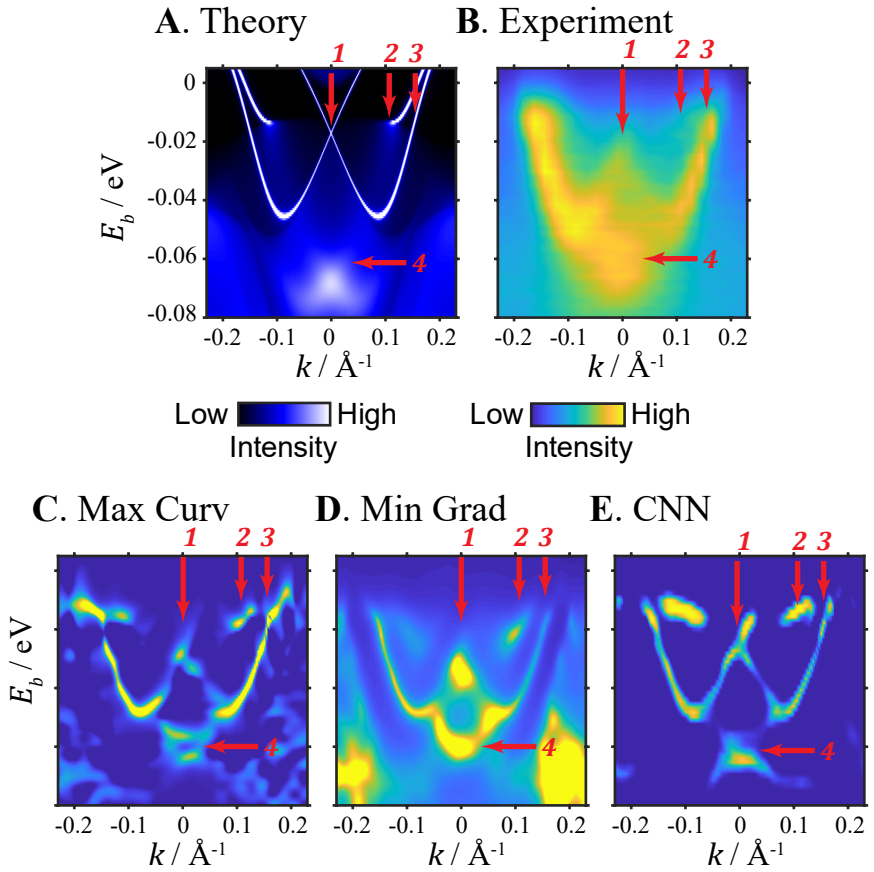

Figure 4.7: Comparison of experiment data, DFT calculation and different data analysis methods. A. Density functional theory calculation of the band structure of $NbIrTe_4$. The three bands crossing the Fermi energy (E_F) are marked with red arrows. The fourth arrow marks the crossing below the Fermi surface. The brighter color shows higher intensity. **B.** The corresponding experiment data of the band structure. The data is used to produce the subsequent results in C – E. The four red arrows mark the corresponding features in A, which is blurry in the experiment. The yellow color shows high intensity while the blue color shows the low. **C. - E.** The result of Maximum Curvature (C), Minimum Gradient (D), and the CNN (E) methods that extract the energy band from the experiment data in B. Interpolating and smoothing are used for pre-processing.

4.4.2 Benchmark with experiment data

To evaluate the performance of our algorism in experiment data, an example of the 2D experimental dispersion from sample $NbIrTe_4$ is presented in Figure 4.7. For reference, the theoretically calculated energy band is shown at Figure 4.7.A in comparison with the experiment data in Figure 4.7.B. The key feature shown in the calculation is that there are three energy bands crossing the Fermi level (E_F) and the band No.2 terminates around E_F and merges with other faint bands. In

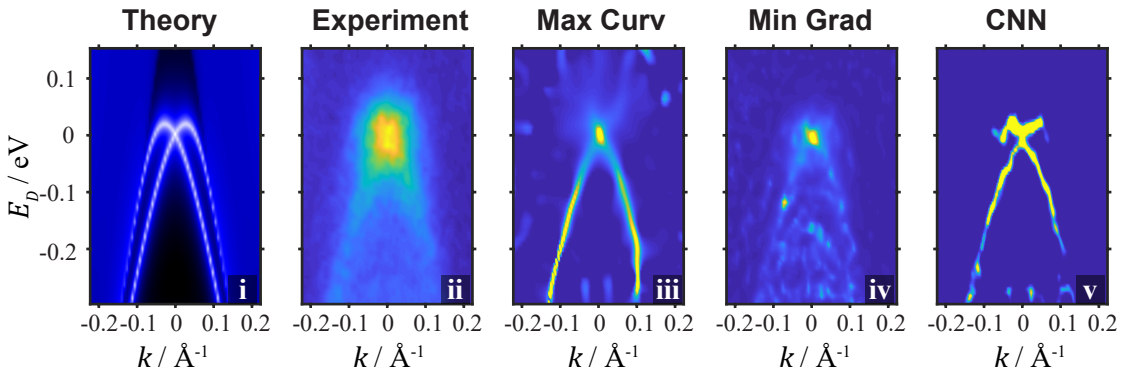

Figure 4.8: Performance analysis of different algorithms with experiment data from $PtSe_2$. Results for the experiment data of PtSe2 band structure. **i.** Theoretical calculation, showing a crossing at the binding energy $E_D = 0$ eV. **ii.** Experiment data. **iii. - v.** The energy band extraction result based on the experiment data, using the method of Maximum Curvature (iii), Minimum Gradient (iv) and CNN (v).

addition, band No. 1 has a degenerate point at $k = 0$ about 60 meV below the E_F. Ideally, a successful data analysis algorithm should resolve all these features from the ARPES intensity map.

Due to the experiment restriction, the number of pixels in the current data along k-direction is only 29. The low resolution makes it even more difficult to directly track the features from the experiment data. The Maximum Curvature (MC) and Minimum Gradient (MG) methods show significant enhancement of the energy band features (as shown in Figures 4.7, C and D) but are either noisy (MC) or still blurry (MG). The result of our CNN method is shown in Figure 4.7.E, demonstrating all three E_F-crossing bands and the crossings below E_F. It also shows that the band in the middle (No.2) ends at about -15 meV below the E_F, which matches the theoretical calculation.

Another example of the 2D experimental dispersion (from sample $PtSe_2$ in Reference [18]) is used in Figure 4.8. A degeneracy point is expected in the PtSe2 band structure (Figure 4.8.i). The experiment data is too blurry to directly delineate the two bands (Figure 4.8.ii); and neither the Maximum Curvature method or the Minimum Gradient method can resolve the two bands clearly (see Figures 4.8 ii and iii). However, the CNN method can produce clear result showing the two bands crossing without noticeable noise. From these two examples, we show that the CNN

method can achieve comparable or better performance than the traditional methods, especially in the resilience to the noise and sharpness of the resulting features.

4.5 Discussion and conclusion

To understand the mechanism of the CNN method, the filters and responses from the first layer are visualized in Figure 4.9. Some of the filters (e.g. filters No. 1 and 2) are sensitive to the inclined ridges; some of the filters are sensitive to flat bands (e.g. filter No. 3); some of the filters act like 'background detector', which separate the band and the noisy background (e.g. filter No. 4); and some of the filters act as a convolution along the vertical axis (e.g. filter No. 5), which is similar to the traditional energy-momentum curve peak finding method [4]. In the second layer, these feature maps are averaged with weights and finally used to reconstruct the sharp-feature map in the output layer.

The output of the CNN method marks the position of the peaks, which stands for the energy band. However, the information of the self-energy, which is of interest in analyzing the behavior of the correlated system [19, 20], is not extracted. In the future study, this part of information could be included by adding a branch in the neural network. Another limitation of the model is that the generation of simulated training data does not involve any k_z broadening caused by finite mean free path of photoelectrons [1], which will result in unexpected result when this effect is significant. A more carefully designed simulation of the training data can be applied to avoid this issue.

To conclude, in this work, we demonstrate that the CNN method shows good sensitivity to the dispersive features in real ARPES data and the resilience to noise. Our results show that the feature extraction in physics experiment's 2D data analysis can be treated as an image restoration problem in computer vision and can be tackled with convolutional neural network. The training process provides an example that the neural network can be used to solve the inverse problem when the physics model is known. Moreover, this methodology can also be used in general peak hunting from the multidimensional data and can be potentially used in other physical processes.

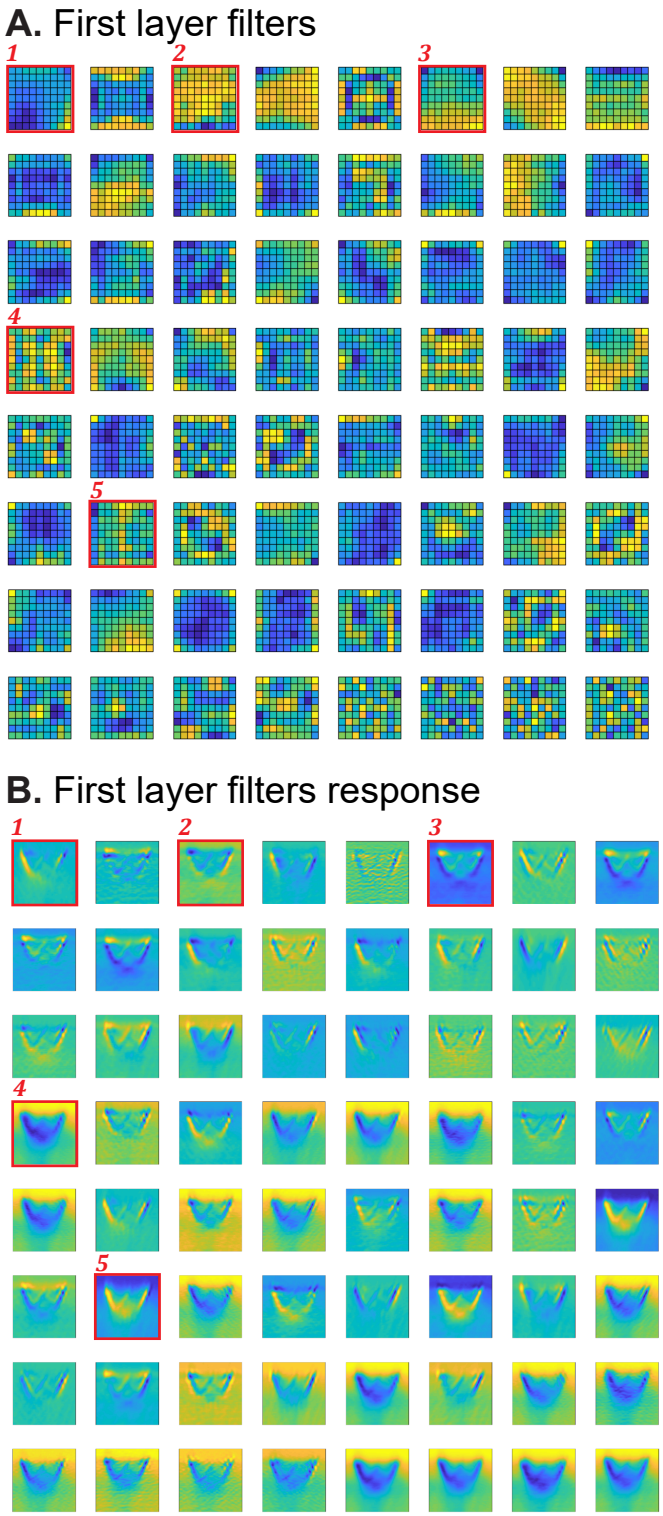

Figure 4.9: The filters and response of the first layer in CNN. A. The 64 filters. The filters are arranged in the descending order of variance. **B.** The response of the filters, which is convolved with the experiment data in Figure 4.7.

Bibliography

[1] Andrea Damascelli, Zahid Hussain, and Zhi-Xun Shen. "Angle-resolved photoemission studies of the cuprate superconductors". In: *Reviews of modern physics* 75.2 (2003), p. 473.

[2] Gerd Binnig and Heinrich Rohrer. "Scanning tunneling microscopy". In: *Surface Science* 126.1-3 (1983), pp. 236–244.

[3] Akio Kotani and Shik Shin. "Resonant inelastic x-ray scattering spectra for electrons in solids". In: *Reviews of Modern Physics* 73.1 (2001), p. 203.

[4] P. Zhang et al. "A precise method for visualizing dispersive features in image plots". In: *Review of Scientific Instruments* 82.4 (2011), p. 043712. URL: https://www.ncbi.nlm.nih.gov/pubmed/21529018.

[5] Yu He, Yan Wang, and Zhi-Xun Shen. "Visualizing dispersive features in 2D image via minimum gradient method". In: *Review of Scientific Instruments* 88.7 (2017), p. 073903.

[6] C. Dong et al. "Image Super-Resolution Using Deep Convolutional Networks". In: *IEEE Trans Pattern Anal Mach Intell* 38.2 (2016), pp. 295–307. URL: https://www.ncbi.nlm.nih.gov/pubmed/26761735.

[7] Christian Ledig et al. "Photo-realistic single image super-resolution using a generative adversarial network". In: *CVPR*. Vol. 2. 3. 2017, p. 4.

[8] Dmitry Ulyanov, Andrea Vedaldi, and Victor Lempitsky. "Deep Image Prior". In: *arXiv preprint arXiv:1711.10925* (2017).

[9] Christopher M. Bishop. *Pattern Recognition and Machine Learning*. Springer, 2006.

[10] Y. LeCun, Y. Bengio, and G. Hinton. "Deep learning". In: *Nature* 521.7553 (2015), pp. 436–44. URL: https://www.ncbi.nlm.nih.gov/pubmed/26017442.

[11] Warren S McCulloch and Walter Pitts. "A logical calculus of the ideas immanent in nervous activity". In: *The Bulletin of Mathematical Biophysics* 5.4 (1943), pp. 115–133.

[12] Xavier Glorot, Antoine Bordes, and Yoshua Bengio. "Deep sparse rectifier neural networks". In: *Proceedings of the fourteenth international conference on artificial intelligence and statistics*. 2011, pp. 315–323.

[13] David E Rumelhart, Geoffrey E Hinton, and Ronald J Williams. "Learning representations by back-propagating errors". In: *Nature* 323.6088 (1986), p. 533.

[14] Diederik P Kingma and Jimmy Ba. "Adam: A method for stochastic optimization". In: *arXiv preprint arXiv:1412.6980* (2014).

[15] Chao Dong et al. "Learning a deep convolutional network for image super-resolution". In: *European Conference on Computer Vision*. Springer. 2014, pp. 184–199.

[16] Vinod Nair and Geoffrey E Hinton. "Rectified linear units improve restricted boltzmann machines". In: *Proceedings of the 27th international conference on machine learning (ICML-10)*. 2010, pp. 807–814.

[17] Franklin C. Crow. "The use of grayscale for improved raster display of vectors and characters". In: *SIGGRAPH Computer Graphics* 12.3 (1978), pp. 1–5.

[18] Yiwei Li et al. "Topological origin of the type-II Dirac fermions in $PtSe_2$". In: *Physical Review Materials* 1 (7 Dec. 2017), p. 074202. URL: https://link.aps.org/doi/10.1103/PhysRevMaterials.1.074202.

[19] Haoxiang Li et al. "Coherent organization of electronic correlations as a mechanism to enhance and stabilize high-TC cuprate superconductivity". In: *Nature Communications* 9.1 (2018), p. 26.

[20] W Meevasana et al. "Hierarchy of multiple many-body interaction scales in high-temperature superconductors". In: *Physical Review B* 75.17 (2007), p. 174506.

5

STM image analysis for Bi_2O_2Se

Contents

As graphene is a thin-layer material with high-mobility, the applicability of graphene in fabricating high-performance semiconductor devices is limited due to the absence of a band gap in its electronic structure. Unlike graphene, the recent discovered bismuth-based oxychalcogenide material Bi_2O_2Se has not only the desired high mobility ($> 20\,000\,cm^2/V/s$) but also a moderate energy band gap $\sim 0.8\,eV$. Together with its air-stability and thin-film nature, Bi_2O_2Se has become a promising candidate for the application in fast, low energy consumption and ultra-small electronic devices.

In this work, we present an STM image analysis for the reconstruction patterns on cleaved Bi_2O_2Se surface. Our study reveals the statistical distribution of the surface patterns and explains the formation of the patterns with a tile model.

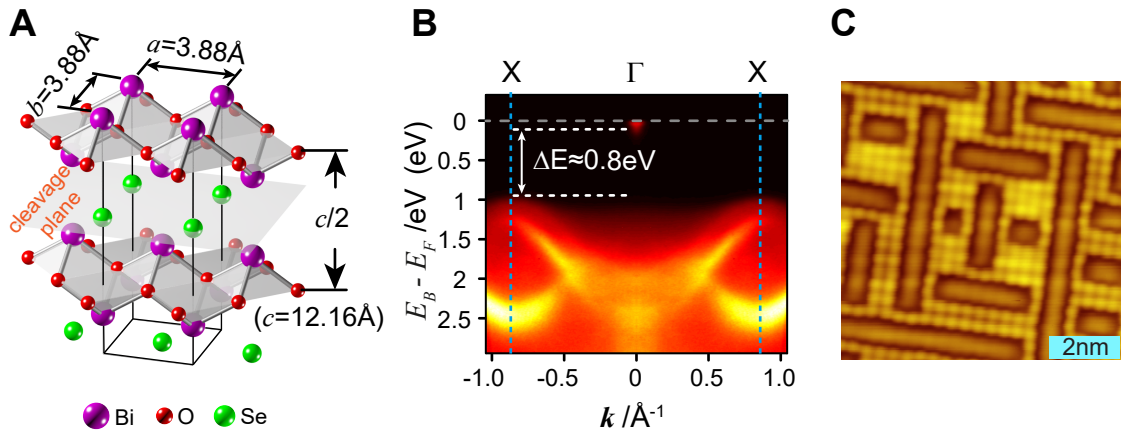

Figure 5.1: Introduction to Bi_2O_2Se. **A.** Illustration of Bi_2O_2Se layered lattice structure. **B.** ARPES data of Bi_2O_2Se showing a band gap ($\Delta E \approx 0.8\,\text{eV}$) between the valence band and the conduction band (the small pocket at Γ point near E_F). Illustration and ARPES measurement by courtesy of Cheng Chen. **C.** Scanning Tunneling Microscope (STM) image showing an 8 nm-by-8 nm area of the cleavage plane. The bright dots are the remaining Se atoms and the dark domains are the vacancies.

5.1 Introduction to Bi_2O_2Se

Recent ARPES and transport study shows that the layered material Bi_2O_2Se is a promising semiconductor for high-performance electronic applications [1]. With its ultra-high mobility ($> 20\,000\,\text{cm}^2/\text{V/s}$), appealing band gap ($\sim 0.8\,\text{eV}$), good air stability, and thin-layer nature, Bi_2O_2Se is suitable for the fabrication of fast, low energy consumption and ultra-small electronic devices [2].

The layered nature of Bi_2O_2Se comes from its crystal structure. As illustrated in Figure 5.1.A, the Bi_2O_2Se layer holds strong covalent bonds. In contrast, the inter-plane interaction is due to relatively weak electrostatic forces, makes the Se-plane easy to break by sample cleavage. The ARPES measurement on freshly-cleaved sample surface reveals an electronic band gap $\sim 0.8\,\text{eV}$ without any in-gap surface state, as shown in Figure 5.1.B. Further ARPES measurement confirms this absence of surface state [3].

To explain the surface electronic structure, Scanning Tunneling Microscope (STM) measurement is performed, which shows the atomic arrangement of the cleavage surface with unusual surface pattern. As shown in Figure 5.1.C and

concluded in Reference [3], the surface consists of Selenium atoms and vacancies. The vacancies form patterns with the width of two atoms along two possible directions that are perpendicular to each other. In this work, we present a statistical survey over the vacancy domains from the STM images. Our results show an exponential decay in the domain length distribution and a equal probability of choosing two orientations. We propose a simple 4-by-4 tile model that can reproduce the patterns with good fidelity and is consistent with the statistical distribution. This model inspires further first-principle study (included in Reference [3]) that shows this configuration only introduces extra density of states in conduction and valence bands while keeping the energy band gap free of surface states.

5.2 STM image analysis for Bi_2O_2Se surface

Before analysing the statistical properties of the domains, an image processing pipeline is designed which segments the vacancies in four 100 nm-by-100 nm STM images.

5.2.1 Methods

By looking at the STM image, one would not expect to mark all the vacancy domains ($\sim$ 2000) purely by hand. But with some image processing techniques, the segmentation of the domain can be achieved automatically.

As shown in Figure 5.2.A, by applying suitable current and voltage, the raw STM image reveals the vacancy domains as bright islands. The image processing task is to segment each individual islands so the subsequent analysis can be performed.

In principle, a binarization process could mark the pixels with intensity values exceeding a certain threshold as 1's and the rest of pixels as 0's. However, the background is varying across the large scanning region, so that a global threshold will not work for all the parts of the entire image. In this case, an adaptive threshold method is calculated, in which the threshold for any pixel depends on the avarage of its neighbors (7px-by-7px region in this case) [4].

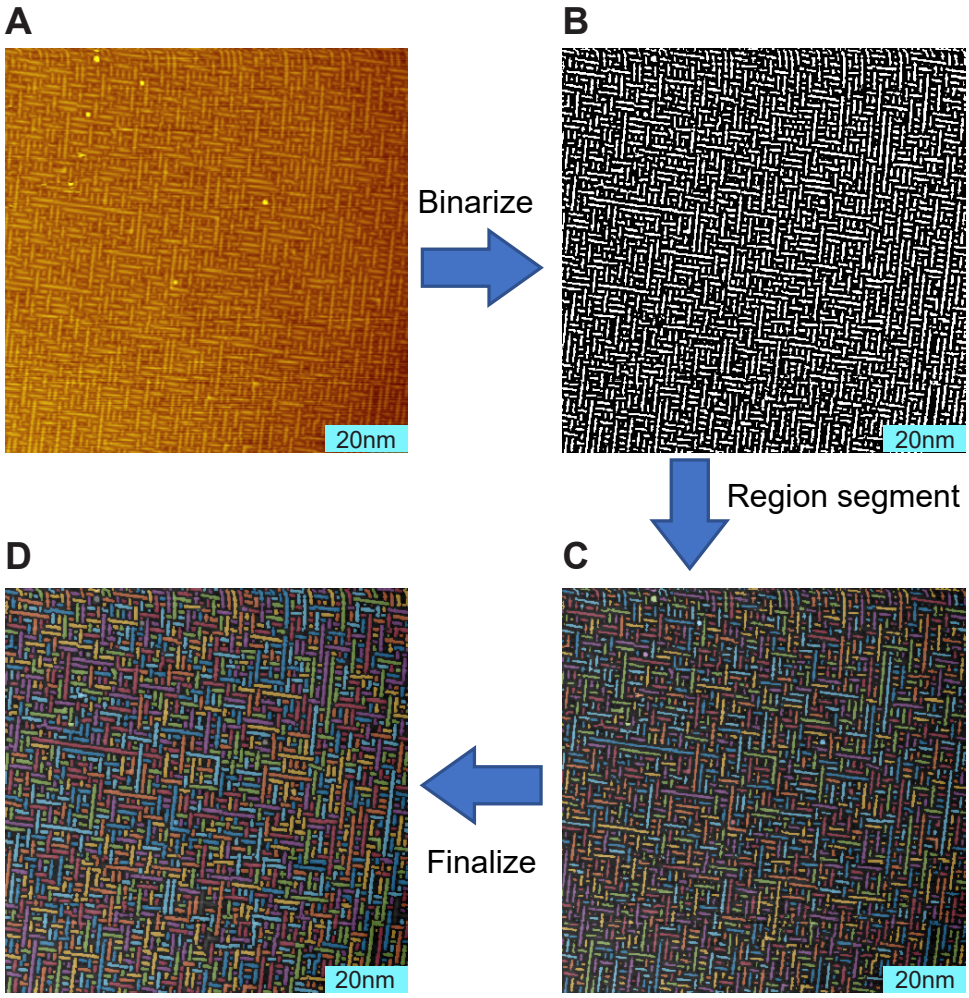

Figure 5.2: Domain segmentation pipeline for STM images of BOS surface. **A.** STM image showing an 100 nm-by-100 nm area of the cleavage plane. The bright domains are the vacancies and the dark part is the remaining Se atoms. **B.** The first step: binarization using an adaptive threshold method. **C.** The second step: label all the individual connected components. **D.** The third step: finalization by image dilation to connect the falsely separated areas.

After the adaptive thresholding, the resulting 0-1 mask is then passed to the algorithm that labels the connected components in the mask [5]. Each labeled connected region is randomly marked with a color for the sake of visual inspection and is presented in Figure 5.2.C.

Some additional conditions, for example the width of the region, are used to exclude the defect areas. To finalize the result, an image dilation is applied to reconnect the falsely separated regions [6].

5.2.2 Results

Figure 5.3 shows four 100 nm-by-100 nm STM images and the corresponding segmentation results. The four images are passed to the same pipeline with little adjustment of parameters. By comparing the segmentation results with the raw images, we find the pipeline shows good stability even with different image qualities and different background variations. Only a small number of vacancy domains are excluded which is difficult to separate even by human eye.

After segmentation, further statistical analysis of the length and orientation distribution for the vacancy domains reveals the hidden properties of the domains.

There are 7902 domains counted in the image to produce the length distribution histogram and 5172 of them are long enough to determine the orientation. The length distribution is presented in Figure 5.4.A, showing the probability that a domain possesses a specific length decays in a exponential-like trend. The length is shown in 'unit-length', which is the lattice constant of Bi_2O_2Se, or the distance between two Se atoms. The orientation distribution in Figure 5.4.B shows that the domains are arranged along the two perpendicular crystal axis with equal probability.

More interestingly, by looking closely at the length distribution graph, a few 'steps' are found in the distribution graph. For example, the 2, 3, 4 and 5 unit-length domains appear in nearly the same frequency, while the 6-atom domain's frequency of occurrence drops to about half of that of the former group. The 6, 7 and 8 unit-length domains form the second platform and the frequency drops again in the 9-atom domains. Similarly, the third step is for the 13 unit-length domains. This interesting phenomenon will be explained by a tile model in the next section.

5.3 Tile model for the surface pattern

5.3.1 Motivation

The motivation of the tile model comes from the observation of the statistic result. The main features summarized from the length and orientation distribution graph are:

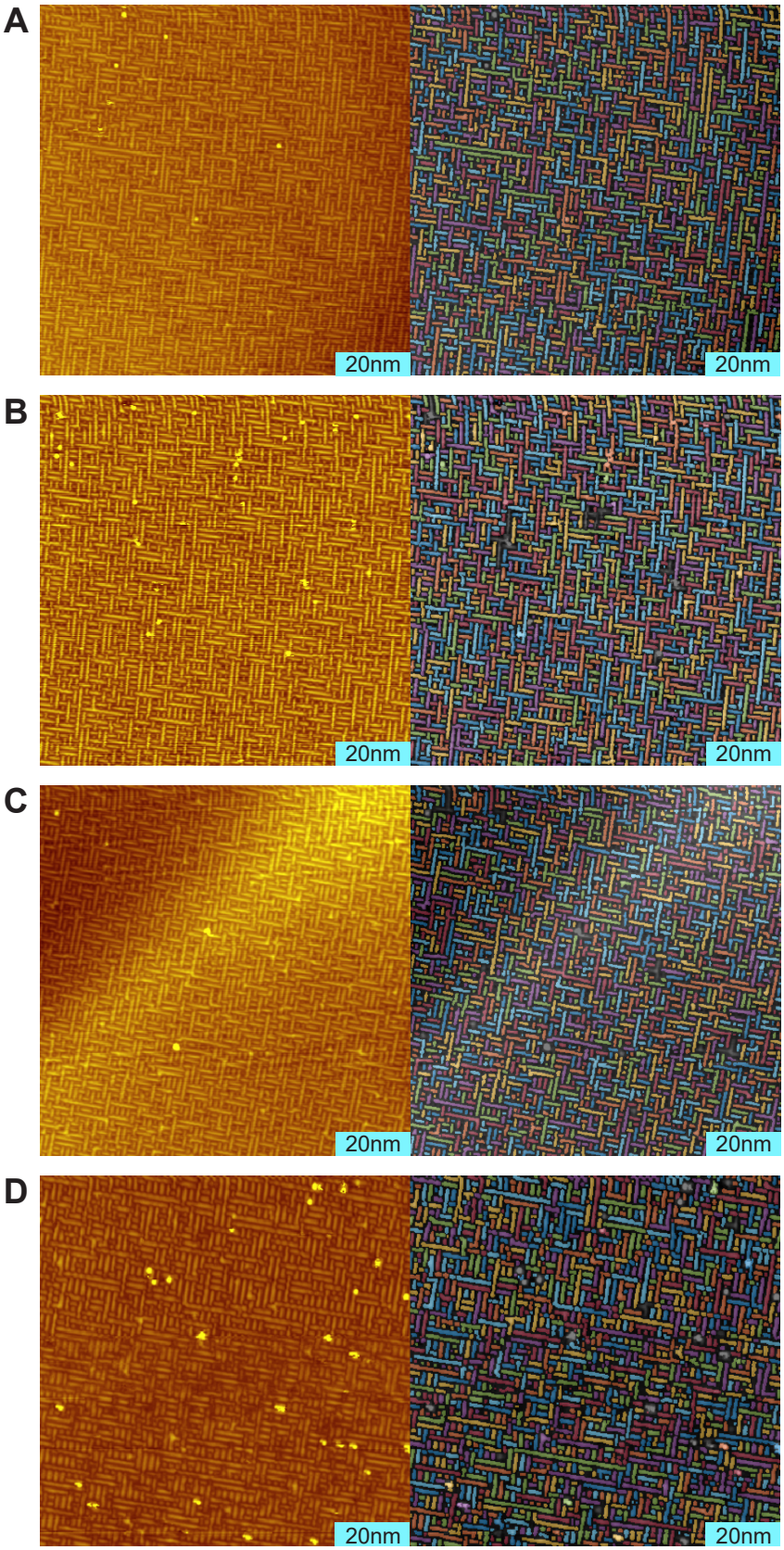

Figure 5.3: The domain segmentation result for four 100 nm**-by-**100 nm **regions.**

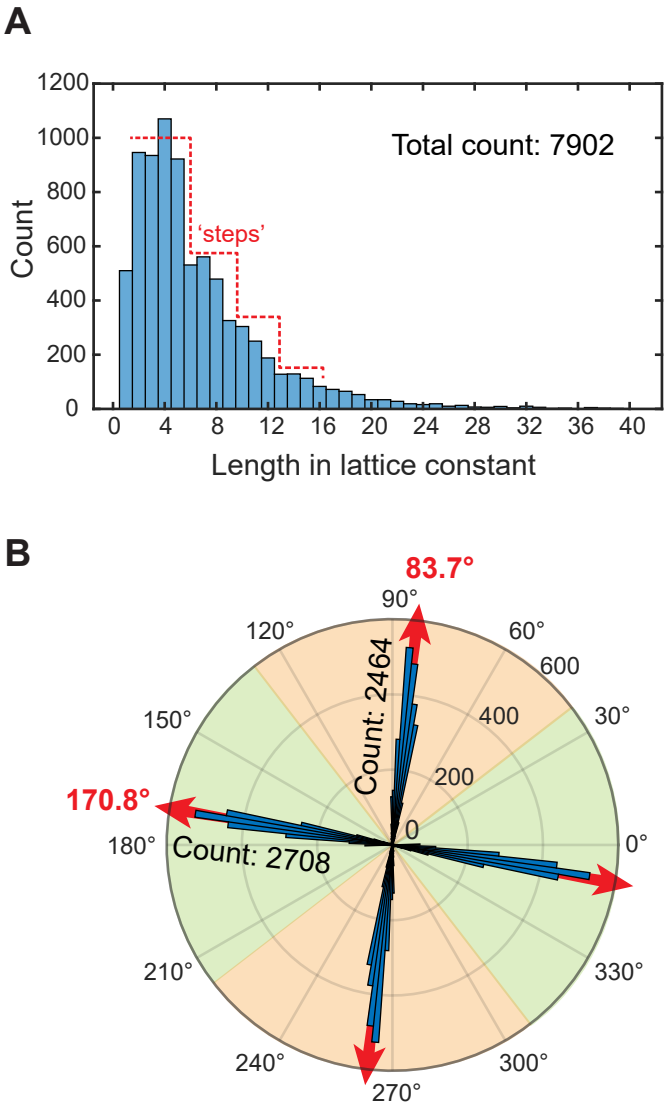

Figure 5.4: Statistics for the segmented vacancy domain. A. Histogram for the length distribution of the vacancy domains. In total, there are 7902 vacancy domains found in the four areas shown in Figure 5.3. The x axis is the length in the unit cell size of the crystal, which is 0.381 Å by measuring the average lattice size in Figure 5.1.C. The distribution shows a step-like shape (marked by a dashed red line) with the first step at around the 5-atom length, the second at the 8- to 9-atom length and the third at the 12- to 13-atom length. **B.** Histogram for the direction distribution of the vacancy domains. In total, there are 5172 domains that are long enough (> 1.4 nm or 3.6 atoms) to determine the direction. Two major axis are found with roughly the same count for each group. The directions counted as X-direction (170.8 deg) are marked with the green background and the directions counted as Y-direction (83.7 deg) are marked with the orange background.

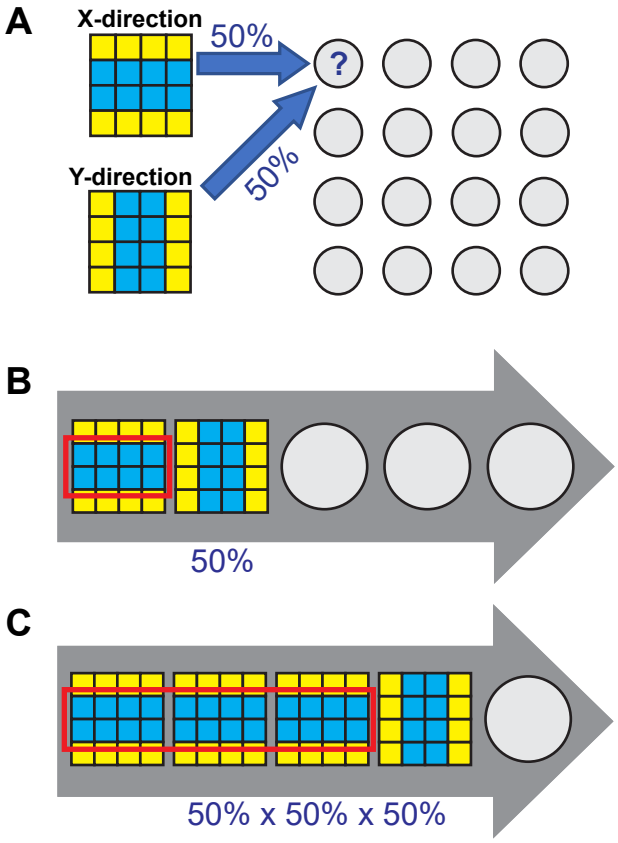

Figure 5.5: Illustration for the tile model. A. Illustration for two basic tiles. One is along the X-direction and the other is along Y-direction. Each tile consists of 4-by-4 atoms, including vacancies (blue squares) in the center and occupants (yellow squares) on the sides. Each tile of the lattice has equal chance (40% for each scenarios) to select one configuration. **B.** Illustration of the formation a 4-atom length X-direction vacancy domain (marked by the red rectangle). While the first tile is taken by an X-tile, the second has 50% probability to be taken by a Y-tile, which has 50% probability to end the growth of the vacancy domain. **C.** Illustration of the formation a 12 unit-length X-directed domain (marked by the red rectangle). While the first, second and third tiles are taken by an X-tile, the second is taken by a Y-tile, which ends the growth of the vacancy domain. Given that the first tile is taken by X-tile, the probability that 'the second and third are taken by X-tiles and the fourth is taken by Y-tile' is $50\% * 50\% * 50\% = 12.5\%$.

1. Detailed morphology from Figure 5.1:

   (a) The X-direction domain and Y-direction domain do not cross and are separated by one unit-length.

   (b) The parallel domains are separated by two unit-lengths.

2. Statistic from Figure 5.4:

(a) The orientation of the domains are either along X or Y, with 50% probability, respectively.

(b) The frequency of occurrence of domains with certain length halves for every 4 or 3 unit length.

These features can be captured by a simple tile model. The assumptions are that the Se atoms and vacancies form into basic 4-by-4 tiles, as shown in Figure 5.5.A. A basic X-direction (or Y-direction) tile consists of two middle rows (or columns) which are vacancies and the other two bilateral rows (or columns) which are occupancies. The crystal surface is reconstructed with a 4-by-4 super lattice with each site taken by either an X-direction tile or a Y-direction tile, with 50% probability, respectively.

With this arrangement, the probability that a domain extends for one more tile is always 50%. Assuming we have an X-tile domain at the beginning of a row as shown in Figure 5.5.B, the domain has 50% probability to end if the next site is filled with a Y-tile, leaving the domain size 4 unit-lengths. Similarly, for a 12 unit-length domain in Figure 5.5.C, the growth is involved a second X-tile (50%), a third X-tile (50%) and a Y tile at the end (50%). The probability for this incident is $(\frac{1}{2})^3$. We can conclude that the probability of having a domain with n-tiles will be $(\frac{1}{2})^n$. More strict mathematical treatment is needed for 2D image because a domain can be extended along both ends, but the conclusion remains the same.

5.3.2 Simulation and comparison with experiments

Using this simple tile model, we perform a Monte-Carlo simulation to reproduce the real surface patterns. The results capture several important experimental features. Figures 5.6, A and B shows good visual similarity. By checking the details in zoom-in images in Figures 5.6, C and D, we find that the X-direction domains and Y-direction domains do not cross and are separated by two remaining Se atoms. The parallel domains are also well separated by two unit-lengths. However, it can be found that in the STM image (Figure 5.6.D) there are vacancy domains separated by three unit-lengths, which cannot be found in the simulation. This discrepancy may be due to imperfections in the formation of the unit tiles in experiment.

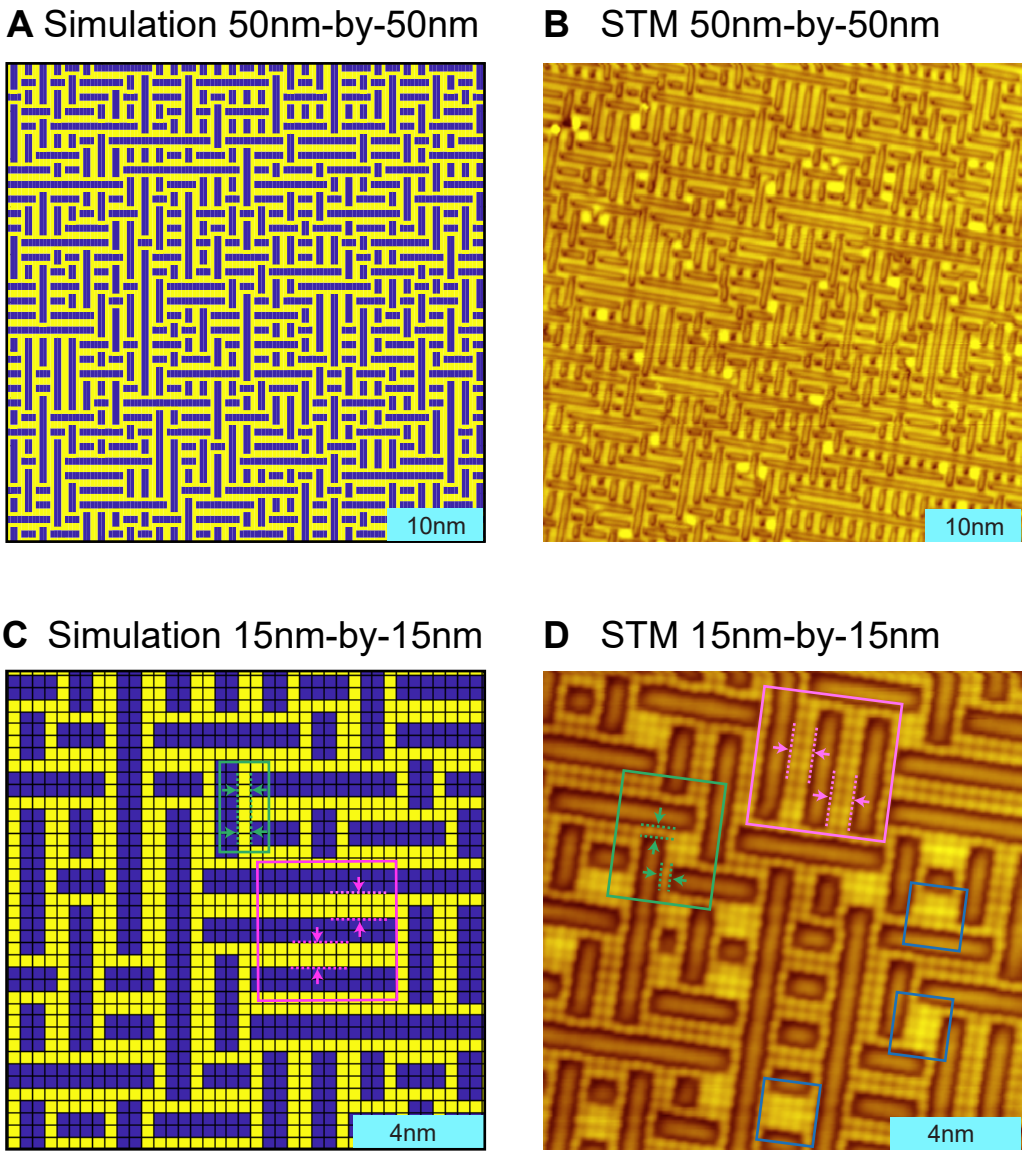

Figure 5.6: Result of Monte Carlo simulation. A. and **B.** Side-by-side comparison between a simulated 50 nm-by-50 nm area (A) and an STM image of the same size (B). The patterns from the two images are visually similar. **C.** and **D.** Side-by-side comparison between a simulated 15 nm-by-15 nm area (C) and an STM image of the same size (D). The patterns are not only visually similar but also agree in details: the domain width is strictly twice of the lattice constant; the parallel domains are separated by twice of the lattice constant (a pair of examples is marked by pink boxes); the X-direction domains and Y-direction domains do not cross and are separated by two atoms (a pair of examples is marked by green boxes.) The blue rectangles in D mark the occupancies with odd number of unit-lengths that could not be found in the simulations.

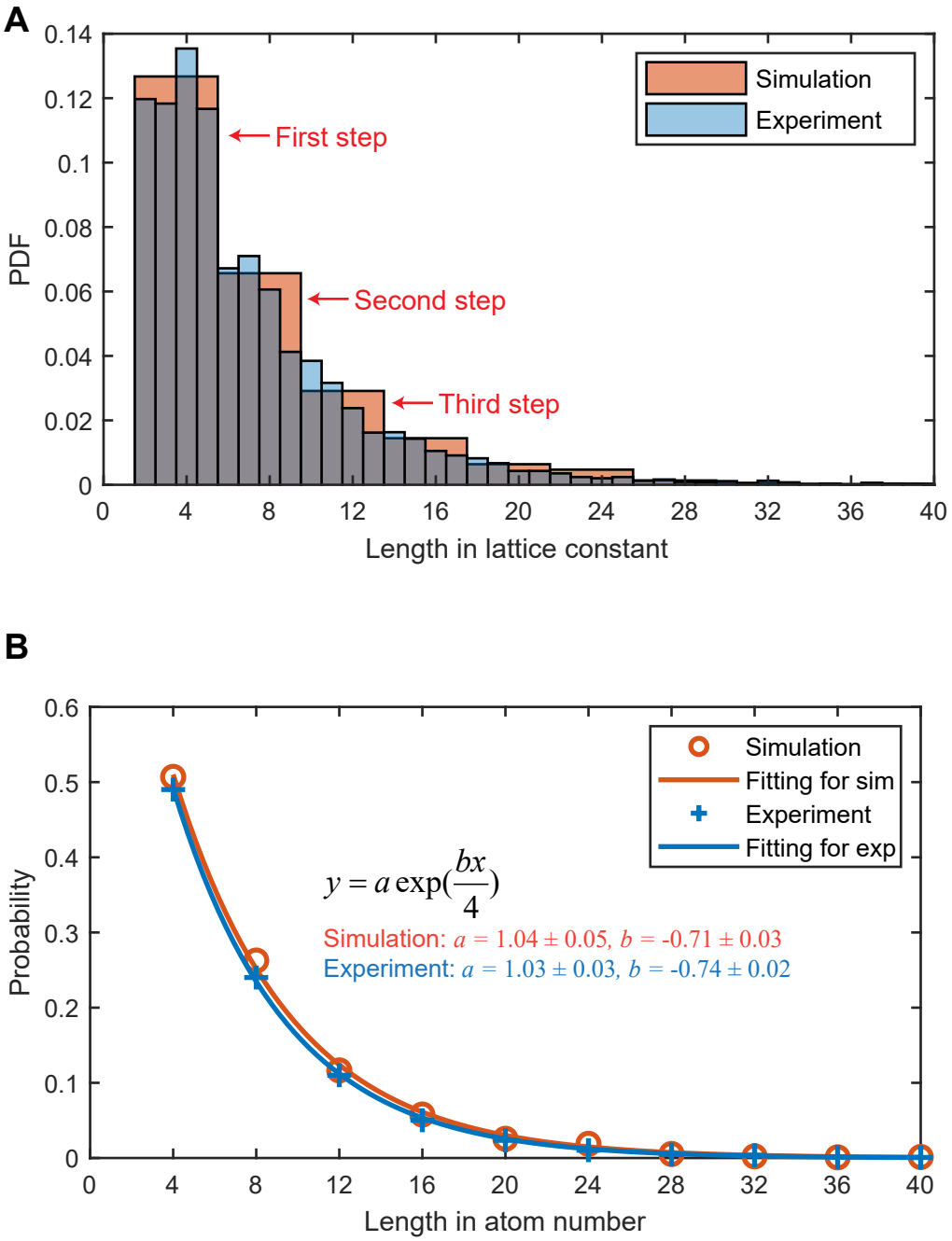

Figure 5.7: Statistic analysis for the simulation and the experiment results. **A.** Histogram for the length distribution in the simulated and the experimental images. The source images are about 100 nm-by-100 nm both for the simulation and the experiment to prevent systematic difference due to the presence of image borders. The bin edges of the histogram is $[0.5, 1.5]$, $[1.5, 2.5]$, ... etc. for the experiment and $[1.5, 5.5]$, $[5.5, 9.5]$, ... etc. for the simulation. The histogram is normalized to probability density function (PDF). The steps in the histogram is marked by red arrows. **B.** Fitting of the probability distribution of domain length with an exponential model. For both the experiment and the simulation, the bin edges for each data point is $[1.5, 5.5]$, $[5.5, 9.5]$, ... etc. The fitting result for the simulation is $y = 1.04 * \exp(-0.71 * n)$ and for the experiment $y = 1.03 * \exp(-0.74 * n)$, where n is the number of tiles and $n = x/4$, where x is the domain length in lattice constant.

The statistical analysis further reveals similarity between the simulation and the experiment. As shown in Figure 5.7.A, the histogram of length distribution in the simulated image approximately coincides with the experimental graph. Note that the assumption of the tile model restricts the length of the domain to be a multiple of 4 unit-lengths. By adjusting the bin-edges to match the observed 'steps', we could conclude that domains with 0.5 to 5.5 unit-lengths correspond to one-tile configurations (with 4-by-4 sites); similarly, domains with 5.5 to 8.5 and 8.5 to 12.5 unit-lengths correspond to two-tile and three-tile configurations, respectively. One may ask why most of the domains do not take exact 4, 8 and 12 unit-lengths. We argue that this may be due to 1) the imperfect tiles observed in Figure 5.6.D and 2) the segmentation algorithm inaccuracy.

Recalling that in Section 5.3.1, we mentioned that any domain has the probability of $(\frac{1}{2})^n$ to be an n-tile domain. The fitting using the statistic result of length distribution from both the simulated images and the experimental STM images shows that the probability y is an exponential function of the tile number n. The fitting parameters are consistent between the simulated results and the experiment results.

For the simulation,

$$y = a\exp(bn) = 1.04 * \exp(-0.71 * n) = 1.04 * (0.49)^n$$

For the experiment,

$$y = a\exp(bn) = 1.03 * \exp(-0.74 * n) = 1.03 * (0.48)^n$$

Note that the coefficient in front of the exponential is slightly larger than 1 and the decaying factor is smaller than 0.5. This is because the image border cuts the longer domains, so the fitting results are systematically biased for smaller domains. In fact, larger-scale fitting results show that $a = 1.028 \pm 0.010, \exp(b) = 0.493 \pm 0.006$ for an area of 200 nm-by-200 nm and $a = 1.003 \pm 0.007, \exp(b) = 0.500 \pm 0.011$ for an area of 400 nm-by-400 nm, which are closer to $\exp(b) = 1/2$.

5.4 Discussion and Conclusion

The proposed tile model clearly reproduces the vacancy pattern of Bi_2O_2Se cleavage surface and shows consistence in statistical distribution. The 4-by-4 tile matches the 4-unit-length steps found in the statistical results of the STM images. As we provide a highly possible configuration that explains the origin of the surface pattern, further first-principle computation is able to be performed in Reference [3] which explains the absence of the surface state in the energy band gap.

Bibliography

[1] Jinxiong Wu et al. “Controlled synthesis of high-mobility atomically thin bismuth oxyselenide crystals”. In: *Nano Letters* 17.5 (2017), pp. 3021–3026.

[2] Jinxiong Wu et al. “High electron mobility and quantum oscillations in non-encapsulated ultrathin semiconducting Bi_2O_2Se”. In: *Nature Nanotechnology* 12.6 (2017), p. 530.

[3] Cheng Chen et al. “Electronic Structures of a High-Mobility Layered Oxychalcogenide Semiconductor, Bi_2O_2Se”. In: *S* (2018).

[4] Derek Bradley and Gerhard Roth. “Adaptive thresholding using the integral image”. In: *Journal of Graphics Tools* 12.2 (2007), pp. 13–21.

[5] Robert M Haralick and Linda G Shapiro. *Computer and robot vision*. Addison-wesley, 1992.

[6] Rafael C Gonzalez. *Digital image processing*. Prentice hall, 2016.

6
Discussion and Conclusion

We have demonstrated that micro-ARPES has the sample morphology mapping ability that can be used to resolve the electronic structure spatially in various domains with few-layer graphene on a copper substrate as a model system. We find that the layer-wise absorption rate of photoelectrons is 54%. As a result, the micro-ARPES can detect the band structures for up to five-layers. In addition, we report a substrate doping effect and explain the layer-dependence of the doping effect using an effective capacitor model.

Deploying this real-space scanning ability, we investigate the energy band structure of twisted bi- and trilayer and graphene with evolving twist angles. We find that the van Hove Singularities (vHS) exist in large regime of twist angle (from 5.4° to 31.6°), resulting in a wide tunable binding energy range over 2 eV. We also observe multiple vHSs at different binding energies in trilayer graphene. With the large tuning range of vHS binding energy, twisted multilayer graphene provides a promising material base for optoelectrical applications with wavelength selectivity. While our micro-ARPES study establishes a systematic picture of the electronic structure evolution in large twist angles, future investigation is needed for the small twist angle scenarios which possesses rich physics.

To further empower the ARPES experiment data analysis, we propose a convolutional neural network (CNN) based method to extract the energy band

features from 2D data. This three-layer CNN model that is trained with simulated data generated by a physical model shows good sensitivity and noise resilience when applied to the dispersive features in real ARPES data. Our results demonstrate that the neural network is suitable to solve the inverse problem for interpreting scientific data. This method can be generalized to other experiments in which the physical process is clearly modeled while the data is challenging to interpret.

Finally, we use STM to investigate the surface reconstruction of the layered material Bi_2O_2Se. We discover a strip-like Se-vacancy arrangement of the cleavage surface according to the microscopic images. Further statistical study reveals an exponential decay in the domain length of the vacancies. Our tile model explains the formation of this surface pattern and provides a configuration that counts for the absence of any in-gap surface states in Bi_2O_2Se electronic structure.